High-Dynamic Range Collision Detection using Piezoelectric Polymer Films for Planar and Non-planar Applications

by

James Michael Wooten

A thesis submitted to the Graduate Faculty of
Auburn University
in partial fulfillment of the
requirements for the Degree of
Master of Science

Auburn, Alabama
August 3, 2013

Keywords: piezoelectric, polymer, collision detection, PVDF, robotics

Approved by

David M. Bevly, Co-Chair, Professor of Mechanical Engineering
John Hung, Co-Chair, Professor of Electrical and Computer Engineering
Dan Marghitu, Professor of Mechanical Engineering

Abstract

This thesis develops a large area collision detection system utilizing the piezoelectric effect of polyvinylidene fluoride film. Complex high speed autonomous articulations associated with modern large-scale high degree-of-freedom (DOF) robotic arms have a high possibility of collision when integrated into human cooperative environments for human-aid, task automation, and biomedical interfacing. The proposed system provides high dynamic range for sensation and robust adaptability to achieve collision detection on complex surfaces in order to augment robotic systems with collision perception. The design allows for increased cohabitation of human and high DOF robotic arms in cooperative environments requiring advanced and robust collision detection systems capable of retrofitting onto deployed and operating robotic arms in the commercial world. Sensor testing is accomplished using multiple collision stimuli to mimic real world performance as well as impact force modeling utilizing high speed cameras. The experimentation results show a wide dynamic sensing range for collision force, from $5\,\mathrm{N}$ to $300\,\mathrm{N}$ and consistent sensor response for planar and non-planar applications. The thesis will show and support the sensor capability of wide range of collision detection while maintaining adaptability of sensor design to multiple scenarios. The approach differs from current work which primarily focuses on small-range low levels of tactician perception, small area sensor requiring complex construction, and associated electronics and processing complexity for common approaches. The pseudo-membrane design eliminates the construction complexity and limited application scope while achieving high and low levels of collision detection utilizing simple electronics and processing method. The captured experimentation results highlight the consistency of response for multiple applications, standard deviation of results less than $1\,\mathrm{GPA}$, and the large range of collision detection capability from $5\,\mathrm{N}$ to $300\,\mathrm{N}$.

Acknowledgments

<p style="text-align:center">Table of Contents</p>

<p style="text-align:center">iv</p>

List of Figures

List of Tables

List of Abbreviations and Nomenclature

ϵ Strain

γ Shear Strain

σ Stress

τ Shear Stress

E Young's Modulus

G Shear Modulus of Elasticity

Q Charge

ADC   Analog to Digital Converter

ak   daton

DOF   Degree-of-freedom

PVDF   Polyvinylidene Flouride

Chapter 1

Introduction

Complex high speed autonomous articulations associated with modern large-scale high degree-of-freedom (DOF) robotic arms have a high possibility of collision when integrated into human cooperative environments for human-aid, task automation, and biomedical interfacing. This thesis details a large area collision detection system utilizing the piezoelectric effect of polyvinylidene fluoride film. The design, testing, and results in the following chapters will involve a novel sensor design approach and simple electronics based collision sensing solution for complex planar and non-planar surfaces in non-standard working environments. The sensor design provides high dynamic range for sensation and robust adaptability to achieve collision detection on complex surfaces in order to augment robotic systems with collision perception. The design and electronics presented allow for increased cohabitation of human and high DOF robotic arms in cooperative environments requiring advanced and robust collision detection systems capable of retrofitting onto deployed and operating robotic arms in the commercial world.

The majority of sensing applications rely on a film membrane [1] or pressure [2]. A membrane approach leads to practical concerns for large-area and high impact applications because of physical limitations and a high level of design complexity for large sensor applications and networks. Pressure based designs require more complex electronics and construction to achieve flexibility because of the low signal response and need for a stiff substrate to achieve pressure dynamics. In this thesis, a novel sensor design is suggested utilizing a flexible substrate to allow the film to operate in a pseudo-membrane configuration that can achieve high dynamic range, simplified electronics, and robust applicability. Sensor robustness means that the sensor can operate in a wide variety of environments including but not

1

limited to high and low impacts, non-uniform and complex surfaces, mobile and stationary systems, and human and non-human inhabited. The proposed sensor construction allows for complex shape and non-planar surface applications. The design is intended for safety and control applications related to human-robotics interaction in cooperative environments, arm autonomy in high DOF arms in changing scenarios, and technology redundancy to minimize risk related to collision. Current safety standards limit the amount of force that a robot can impart to a human being as 150N [3]. The proposed sensor provides a dynamic sensing range of 5N to greater than 200N in an effort to detect a state of collision before significant force has been imparted to the object.

1.1 Thesis Outline

This thesis will discuss the design and testing of a pseudo-membrane collision detection sensor utilizing the piezoelectric effect of PVDF film. Some initial information will be presented to give the reader a more thorough understanding of the subject matter. The following chapters of the thesis will progress through the design and modeling of the collision sensor, detail the experimental prototypes built and methods for testing, discuss and present the results from experimentation, and finally conclude the work stating the contributions as well as future work possibilities. The sensor design detailing the polymer selection and construction method will be presented including reference to current sensing designs and drawbacks to available methods. Additionally, the sensor response will be modeled and physical equations presented to convey to the reader an expectation of the sensor functionality. The thesis will then outline and detail the experimentation methods including the hardware for sensor prototypes and interfacing as well as testing setup for collision stimuli. Finally, the results from experimentation methods will be presented including analysis of sensor response to a large dynamic range of collision stimuli. Analysis of results is included to relate sensor response to modeling performed in the design chapter of the thesis. Following the results, the conclusion will highlight the work performed including the contribution of the design and analysis as

2

well as present future work associated with the sensor design. The conclusion will also cover the sensor advantages and contribution to the field will be highlighted.

1.2 Contribution

The sensor design allows for complex planar and non-planar applications. The sampled results show the following characteristics:

- high dynamic sensing range for collisions

- simple construction for ease of application to existing and future systems

- does not require rigid mountings or free space

- rigidity of surface is not a primary factor in response dynamics

- tactile shape and size is limited only by manufacturing technologies

- current technology allows for easily producible collision sensors based on the design and available parts

The thesis work specifically contributes to state of the art work by:

- Design and modeling for pseudo-membrane collision detection sensor.

- Provides for large area capabilities and robust applicability in contrast to membrane based approach [1], flexible PCB with pressure approach [2], and MEMS based approaches [4].

- Achieves a high dynamic sensing range in contrast to tactile perception [5], limited sensing range [6], and object imaging applications [7].

- Additional testing to support work published previously by the author [8].

Chapter 2

Background

In this chapter, the background information needed for later design understandings will be outlined. First, some initial information on the piezoelectric phenomenon used for sensing is presented and then the specific material and phenomena utilized in the sensor construction is shown. Next, the current work being done for collision sensing and tactition is detailed to provide an accurate understanding of past and state of the art work in the field. The classifications and hazards associated with collision for robotics applications are then presented with specific reference to international working standards and safety studies. Then, the motivations and applications of the sensor presented in the thesis are outlined with example robotic systems as well as general collision sensation. Finally, the coordinate system utilized in the thesis is presented to the reader.

2.1 Piezoelectricity and Ferroelectrics

The word "piezoelectricity" comes from the Greek *piezein*, meaning to squeeze or press; thus, piezoelectricity is electricity related to squeezing or pressure. The phenomena of piezoelectricity was discovered and documented in 1880 by the Curie brothers through experimentation involving application of pressure to plates cut in a direction such that the production of an electric charge was observed [9]. Further quantitative analysis showed the piezoelectric effect to yield charge proportional to the applied pressure to the crystals [9]. This direct piezoelectric effect was also shown to work in reverse, allowing elements to be actuated with electricity. The piezoelectric matrix of constants involving the shear and normal vectors of stress and actuation was studied and detailed using maple, spruce and ash wood samples by Fukada in 1955 [10]. The majority of work with piezoelectricity involves the ferroelectric

4

property of polymers and ceramics. Ferroelectrics are polar materials possessing at least two equilibrium orientations of the spontaneous polarization vector field of electric dipole moments of the material in the absence of external electric fields. The polarization vector may be switched between those orientations by application of an external electric field [11]. In ferroelectric polymers, residual polarization due to the orientation of dipoles is stabilized and contributes to the pyro- and piezoelectric activities [12].

2.2 Polyvinylidene Fluoride

Polyvinylidene fluoride is an inert high impedance polymer which can be formed into sheets as well as other easily manipulable forms and belongs to the ferroelectric polymer family. The chemical structure of PVDF molecules is given by (CH2-CF2). CF2 dipoles are aligned normal to the surface of the film after poling and form a residual polarization [12]. The tensile piezoelectricity in stretched and poled films of polyvinylidene fluoride (PVDF) was first demonstrated and documented by Kawai in 1969 [13]. This discovery triggered widely spread investigations on the pyro-, piezo-, and ferro-electricity of PVDF as well as its copolymers, nylons, and other polymers for many years [12]. Kawai [13] produced the piezoelectric effect in PVDF films by stretching the films at high temperature, $100\,°C$-$150\,°C$, and applying a static electrical field to orient the dipoles. Sensing work with polyvinylidene fluoride (PVDF) film-based sensors includes tactile applications related to robotic skin for finger-tips [6], large area coverage [2], stress sensing for shock-wave measurements [14], deflection sensing [15], object identification [7], and power harvesting [16] to name a few. Recent work with manufacturing has increased viability of PVDF as a flexible and adaptable sensor solution for complex surfaces through MEMS-based fabrications [17] as well as the use of organic transistors to create a highly sensitive pressure sensor [18]. The work by Sekitani et al. [18] shows promising results utilizing organic transistors to boost signal output from PVDF sensors by integrating pre-amp stages to the signal into the flexible polymer. The

reduced need for complex amplifier stages as well as signal loss concerns greatly increase the viability of flexible PVDF-based sensors.

2.3 Collision Sensing Methods

State-of-the-art methods for collision detection in robotics cover a wide variety of methods and technologies, but for this thesis will be classified into subcategories related to robotics and environment interactions as well as human interfacing for control and input. The first category uses knowledge of the statics and dynamics of the system, along with the current inertial or dynamic measurement of the movements, to detect collision. A second category of collision sensing, and the primary concern of this thesis, is the sensor design and implementation for collision detection as well as other tactition implementations. The collision technologies presented provide a point of reference to the reader for determining and understanding the benefits of the sensor design and construction presented in Chapter 3.

2.3.1 Estimation and Control

The estimation of collision using dynamic or inertial sensors inside the arm or system frequently incorporates control algorithms with the estimation. Xia et al. [19] utilizes joint torque sensors on a flexible joint manipulator to estimate and implement control law for collision detection and planning. The collision detection presented is primarily focused on the manipulator or actuator of the robotic arm and precise control of the interaction with objects in an unstructured environment [19]. Je et al. [20] demonstrates collision detection utilizing an observer method which eliminates the need for external torque sensors. The work is again focused on the manipulator end of the robotic arm and primarily with grasp strength and intentional object interactions. The presented results show validity of the observer method using power supplied to the motor, measured by current consumption, related to the expected control input [20]. The main drawback of the estimation and control approach is the required knowledge of the system limiting the applicability; specifically, the work using

torque sensors [19] requires extensive energy and elasticity information of the manipulator while the observer method [20] eliminates complex calculations, but necessitates knowledge of control input for the system. Work performed by Haddadin et al. utilized sensor-based collision detection to limit the force imparted by helper robots in a human-robot interaction environment [3]. Haddadin et al. successfully implemented a collision detection and reaction method which is capable of limiting force imparted by the robot to below 150N [3].

2.3.2   Collision Sensors

The sensor category of collision sensing is further decomposed to high fidelity sensors intended for complex tactition and large area and flexible arrays for more complete coverage. Extensive work has been carried out in the field of high resolution tactition using piezoelectric transducers. Kolesar and Dyson utilized a polymer film array in 1995 to implement a tactile object imaging procedure for recognition of shapes including sharp edges, circle, and slotted screw. [7]. The work integrates a 64 sensor piezoelectric based array into an integrated circuit (IC) and performs pre-charge voltage bias to condition the load response. The experimentation yielded accurate object recognition; however, the tactile sensing elements have a low operating range of $0.00\,\mathrm{N}$ to $1.35\,\mathrm{N}$ [7]. Additional tactition research performed by Fujimoto et al., explored detection of slip with an aim towards implementation of artificial finger skin in robotics applications [6]. The results showed accurate detection of slip for static friction determination as well as the viability for the tactile sensing element to be incorporated in a robotic skin application; however, the sensor processing required complex artificial neural network construction and calibration for the logic which limits the applicability of the design. Yamamoto et al. [5] utilized tactile elements created from PVDF to transmit surface texture utilizing a DSP. The work synchronized a tactile presentation display and tactile element to relay information of texture to a user to tactile telepresentation [5]. The primary sensor focus for the work was high fidelity of texture recognition and the sensors utilized were highly sensitive and specialized–limiting the dynamic range.

Extensive work by Seminara et al. to characterize the applicability of PVDF polymer films for robotics applications showed promise for tactile integration and sensing [21]. The work's primary concern was utilizing PVDF in a pressure-based sensing application to form flexible tactile arrays for robotic skin, and the study showed promising sensing ability [21]. Further work in 2012 by Seminara et al. [2] showed the resulting polymer transducer array created from the design. The tactile array integrated PVDF transducers with flexible printed circuit boards(PCBs) to build large area flexible sensing systems. The study showed an acceptable level of sensation; however, the design requirements of flexible PCBs and limited tactile size caused issues for large complex systems.

2.4   Hazard Classification and Concerns

The primary concern for collision sensing and avoidance is elimination of risk not only to the user and environment but also the robotic system being integrated in dynamic cooperative environments. Collision sensing is utilized to satisfy safety requirements of power or force limiting for a robotic system in a cooperative environment [22]. The ISO standard 10218-1 [22] requires robotic systems to stop when a human is in the collaborative workspace of the system. The workspace of the robot for industrial applications involves a wide cordoned-off safety area; however, the workspace for non-structured environments is often defined to be the mechanical area of the robotic system, including the space contained within the covers and collision sensors of a robotic arm. Examples of non-structured environments include the following: operating rooms, human helper robots in the home, medical imaging applications, and cooperative assembly lines. Collision sensations for standard satisfaction requires th system to limit overrun distance when collision occurs; therefore, detection of collision is more important than specific force measurement. The International Standards Organization's list of potential hazard origins for a robotic systems includes, but is not limited to, the following [23]:

- movements of any part of the robot arm(including back), end-effector mobile parts of robot cell

- rotational motion of any robot axes

- materials and products falling or ejection

- between robot arm and any fixed object

- between end-effector and any fixed object

- unintended movement of machines or robot cell parts during handling operations

The standard for robotic systems in an industrial environment goes on to list the following consequences or damage scenarios for the previous described hazards [23]:

- crushing

- shearing

- cutting or severing

- entanglement

- drawing-in or trapping

- impact

- stabbing or puncture

- friction, abrasion

Major safety concerns exist for robotic cooperation in non-static human oriented environments such as operating rooms, work places, emergency rooms, and medical imaging facilities. The majority of mechanical risks associated with robotics involve unintended touch or collision with objects and humans which creates the potential for harm and damage not only to the human or object but also to the robotic system; consequently, accurate collision detection to alleviate the risk is necessary for increased human and robotics cooperation.

2.5   Motivation and Application

The sensor design and modeling presented in this thesis is primarily focused on elimination of sensor complexity present in state-of-the-art tactition sensors. Ease of use and robust applicability is of more concern for commercial safety systems than highly accurate tactition. With the increased use of complex robotics arms for human aid, simple systems for collision detection are necessary to insure safety of the operator and environment. The robotic system presented in Figure 2.1 shows an autonomous robotic imaging arm manufactured by the Siemens AG corporation. The system meets current safety standards through a mechanical switch and bumper based collision detection approach.
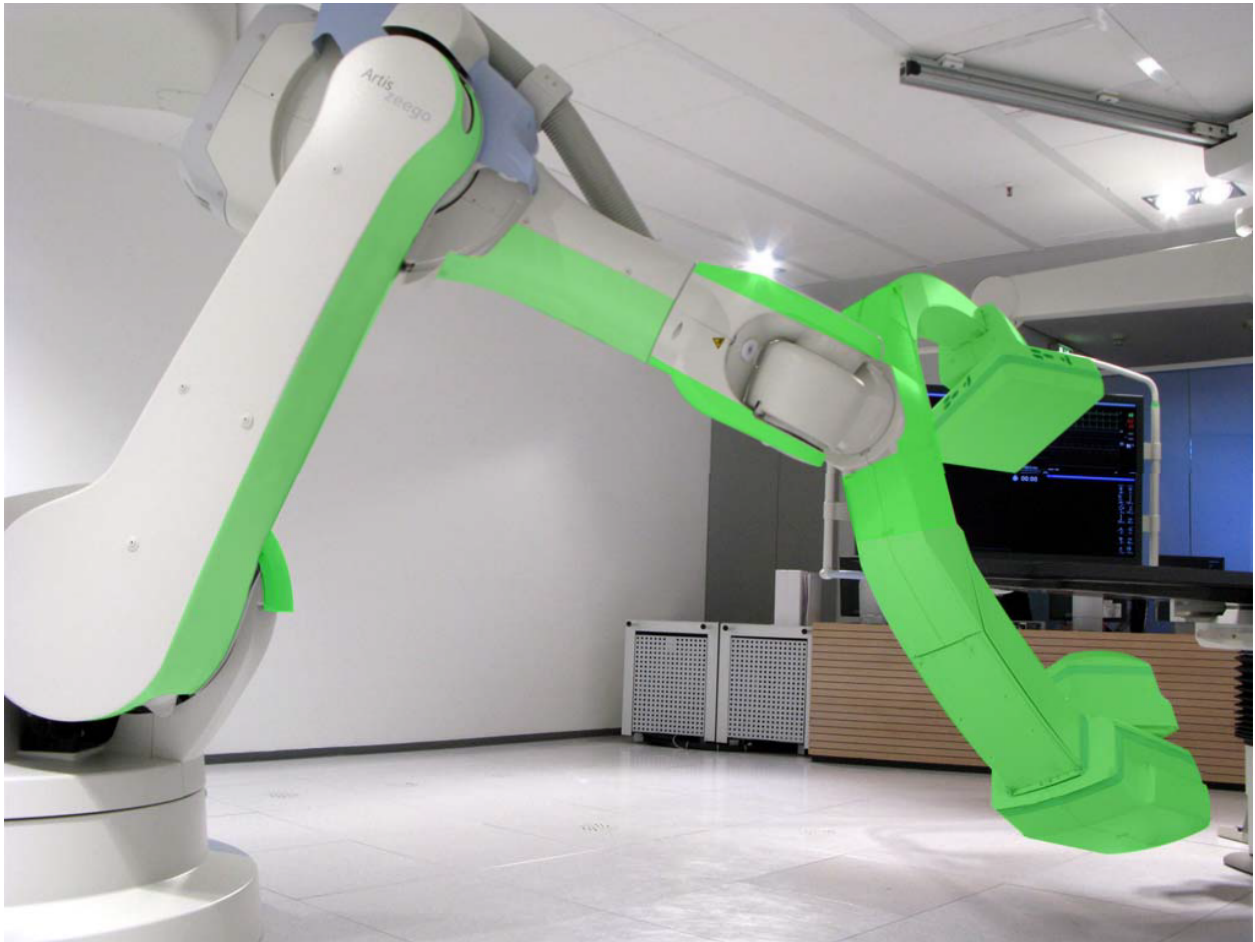
Figure 2.1:   Typical application for sensor design in non-structured environment. The shaded green area on the robotic arm represents desired collision detection areas.

10

Because of high dynamics associated with movement, the mechanical system has issues with false-positives, requires high levels of collision force to generate a detection, and has limited coverage area. The sensor design of the thesis would provide total system coverage of pinch points and other impact areas identified by the green shading in Figure 2.1 while also allowing for collision detection at much lower levels of force in order to reduce damage should collisions occur.

2.6 Coordinate System

{+z, 3, thickness}

{+x, 1, width}
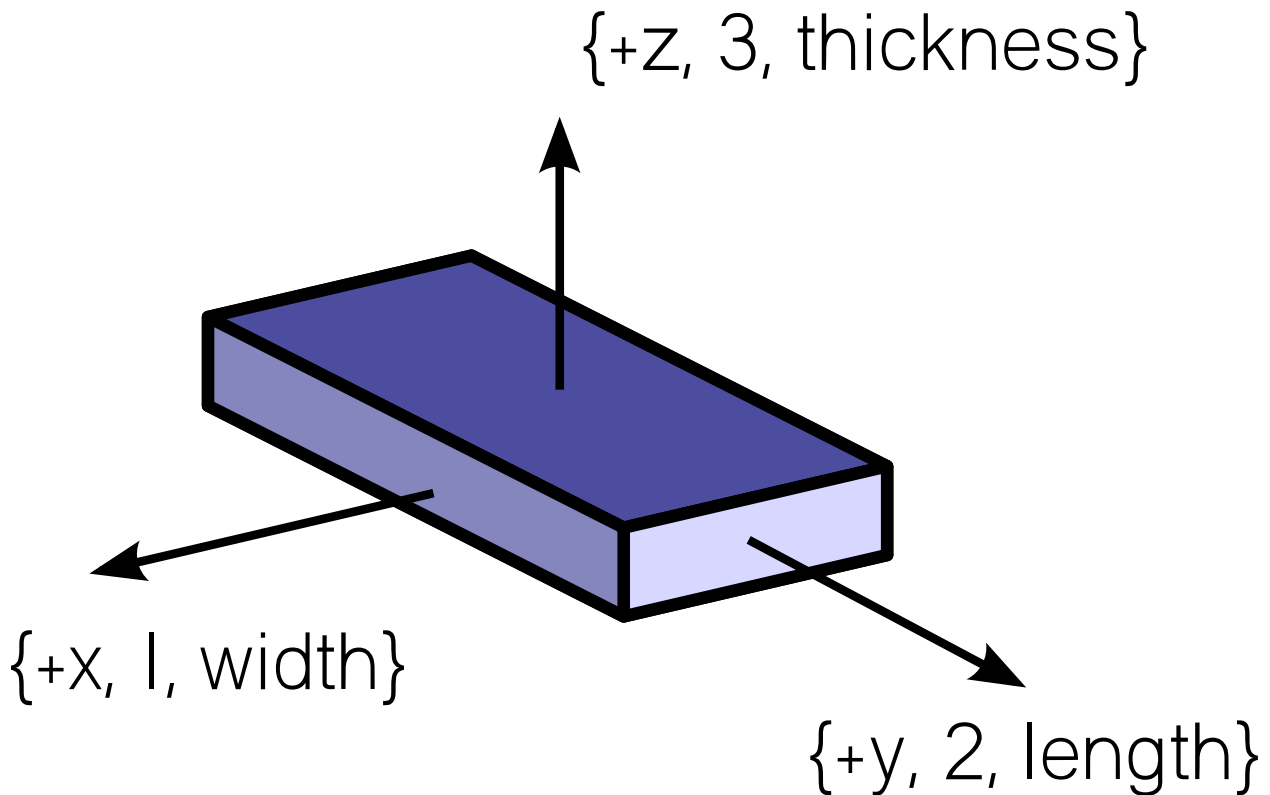
{+y, 2, length}

Figure 2.2: Diagram showing Coordinate System used in Thesis

The Cartesian coordinate system in this thesis uses the following equivalent relations interchangeably, $\{x, y, z\} = \{1, 2, 3\} = \{width, length, thickness\}$. The diagram representing the system for the sensor is shown in Figure 2.2. The *positive z*-axis is normal to the surface of the film and extending away from the film. The *positive x*-axis is extending away from the film as shown while the *positive y*-axis is extending away from the film and aligns

with the length direction of the film. For notational simplicity, the vectors in-line with the axis will use a single notation reducing $xx \rightarrow x$, $yy \rightarrow y$, and $zz \rightarrow z$.

Chapter 3

Design and Modeling of the Collision Sensor

The primary focus of this chapter is the methodology, materials, and functions of the sensor design. By first covering the merits of the materials and structure of the sensor, the reader can more clearly understand the motivations of the design. Next, the electrical effects are explained and modeling of the sensor response to collision is derived to explicate the transduction of the physical model to measured electrical response. Finally, the electronics required for interfacing with and instrumentation of the sensor are detailed.

3.1   Piezoelectric Polymer

PVDF is a piezoelectric and pyroelectric polymer commercially available in thin (<0.1 mm) sheets with uses including force sensors, accelerometer applications, high-frequency resonators, deflection sensing, and many more [15]. The piezoelectric PVDF film is created from homopolymer PVDF sheets which are stretched, heated and simultaneously poled by application of a high voltage field across the film [24]. The stretching aligns the polymer chains of the PVDF and the high voltage orients the dipoles of the chains to create polarization in the film [24]. The polling of the film enables the polymer to generate charge when stressed by heat or physical stress because tensile stress in the film causes the dipoles to flip, creating a charge gradient that generates an electrical displacement. The piezoelectric and pyroelectric effects of the polymer do not significantly degrade over time ($< 1\%$ of original value) ensuring longterm reproducibility of sensations as long as the material is kept below approximately $90\,°C$, depending on PVDF construction. At the Curie point, the poles of the polymer are randomly oriented eliminating the charge gradient [21]. PVDF polymer is uniquely suited to sensor applications due to commercial availability of poled and non-poled

PVDF sheets, readily available construction methods such as extrusion of film, printing of electrodes and sputtering for more fidelity of measurements,, and the material properties of inertness, elasticity and durability.

3.2 Piezoelectric Effect

The proposed sensor utilizes the piezoelectric effect of PVDF thin films to transduce a sensing response to collision with the system. The tactile element transduces experienced stress to an electrical displacement, D, which is the charge density of the film surface, Q/A. The electrical displacement created has additive components of pyroelectric, piezoelectric, and dielectric effects [11]:

$$D = p\Delta T + d_{jk}X_{jk} + \varepsilon E \tag{3.1}$$

The pyroelectric charge is a function of the change in temperature (ΔT) times pyroelectric charge coefficient (p), the piezoelectric charge is a relation of stress applied in Cartesian direction (X_{jk}) with the corresponding piezoelectric charge coefficient (d_{jk}), and the charge related to electric dipole moment is calculated by electric field (E) times the permittivity of the material (ε). For collision sensing, the desire is for electrical displacement, D, to be a purely piezoelectric response, $d_{jk}X_{jk}$. The piezoelectric response is isolated through design and filtering in the following manners. The electric field, E, can be minimized by proper design of the charge amplifier sensor interface in order to eliminate build up of the field. The charge amplifier is discussed in detail later in Subsection 3.7.1. The pyroelectric component, ΔT, can be canceled because of phase orientation of the bilayer sensing element and common mode signal filtering. The elements are placed such that electrodes are reversed on the top and bottom layer resulting in the pyroelectric effect being positive for the upper element and negative for the lower element. The response is out of phase by 180 degrees and the signal can then be filtered by rejecting the common mode of the combined signal. The stress response of the elements is a signed response dependent on the deflection of the film

resulting in isolated piezoelectric response when the films are deflected in the same direction. Therefore, the pyroelectric and dielectric effects fall away reducing (3.1) to the desired purely piezoelectric displacement in (3.2).

$$D = d_{jk}X_{jk} = d_{31}X_{31} + d_{32}X_{32} + d_{33}X_{33} \tag{3.2}$$

The stress vector, X_{jk}, in Equation (3.2) represent tensile stress in length, width, and thickness directions respectively. Due to high compressibility of the substrate relative to the PVDF film, strain related to compression, X_{33} is approximately 0. The piezoelectric constants corresponding to tensile stress in the width and length, d_{31} and d_{32} respectively in Cartesian coordinate representation[1], are equal. Therefore, the electrical displacement of the sensor is proportional to the total transverse and longitudinal stress in the film created by the collision reducing Equation (3.2) further to the reduced representation of the sensor electrical displacement in (3.3).

$$D = d_{31}(X_{31} + X_{32}) \tag{3.3}$$

The applicable material properties of PVDF film are shown in Table 3.1 and provided by the film manufacturer, Measurement Specialties.

Table 3.1: Material Properties of PVDF Film

E	Young's Modulus	$2 - 4 \times 10^9 N/m^2$
d_{31}	Transverse Coefficient	$23 \times 10^{-12} \frac{C/m^2}{N/m^2}$
d_{33}	Compressive Coefficient	$-33 \times 10^{-12} \frac{C/m^2}{N/m^2}$
p	Pyroelectric Coefficient	$30 \times 10^{-6} \frac{C}{m^2 K}$

---

[1]Recall the Cartesian coordinate system in this thesis uses the following equivalent relations interchangeably, $\{x, y, z\} = \{1, 2, 3\} = \{width, length, thickness\}$. The diagram shown previously in Figure 2.2 describes the system in reference to a material sensor.

3.3 Membrane Construction
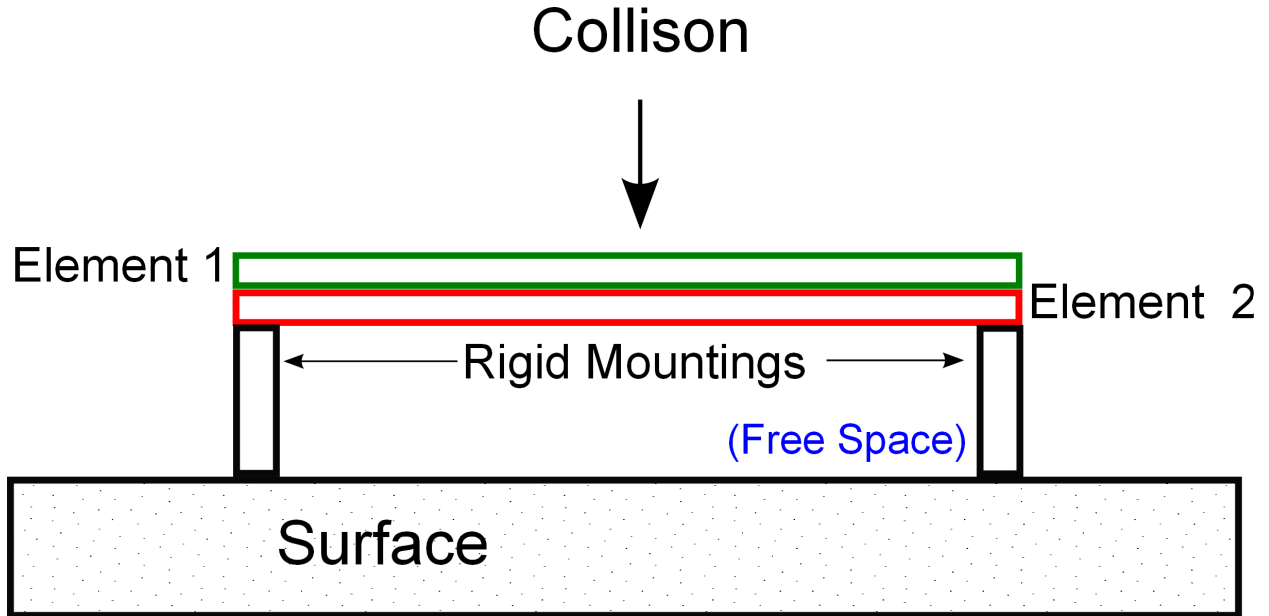
Figure 3.1: Membrane Sensor Construction Diagram

The membrane based construction shown in Figure 3.1 transduces collision to an electrical displacement through stress application to a rigidly mounted membrane. The sensor construction generates stress in tension because of deflection of the membrane from applied force. The equations for modeling the sensation of force collisions are easily derived because the stress, shown in Equation (3.4), is purely a function of the force over cross-sectional area of the film.

$$S = \frac{F}{A_c} \tag{3.4}$$

The pseudo membrane approach involves stress in length and width orientations of the element. The membrane experiences stress in primarily the length direction because increased cross sectional area in the width direction limits the response for membranes with length much greater than the width.

Recall that the piezoelectric effect is a function of the piezoelectric constants and applied stress; therefore, the generated electrical displacement, shown in Equation (3.5), for the membrane approach is congruent to the pseudo-membrane results, discussed later in Section

16

3.6 and shown in Equation (3.19).

$$D = d_{31}S \tag{3.5}$$

Furthermore, the charge (Q) created can be derived by multiplying the electrical displacement, which is a charge density, by the area of the element (A).

$$Q = d_{31}\frac{F}{A_c}A \tag{3.6}$$

System modeling is greatly simplified for the membrane approach. However, the membrane construction method suffers in an application sense because it requires free space for diaphragm deflection and rigid mountings in order to achieve dynamic sensing range. These requirements necessitate specialized construction on an application by application basis, limitation in sensor curvature and reduction of thickness, and reduced durability because the sensor relies on the elastic nature of the film to return to steady state. Large repetitive force application can lead to degradation in performance over time. Therefore, in this thesis the novel approach will utilize a pseudo-membrane construction to eliminate construction requirements while maintaining similar sensing method to a membrane approach.

3.4 Pressure Construction

The pressure-based construction, shown in Figure 3.2, relies on stress created from pressure applied to the sensor. The pressure is generated because the sensor is mounted to a sufficiently rigid substrate or surface such that force applications cause compression of the film elements. The stress(S), shown in Equation (3.7), is now the pressure generated by the collision or the force(F) of the collision over the contact area(A_o) of the object.

$$S = \frac{F}{A_o} \tag{3.7}$$
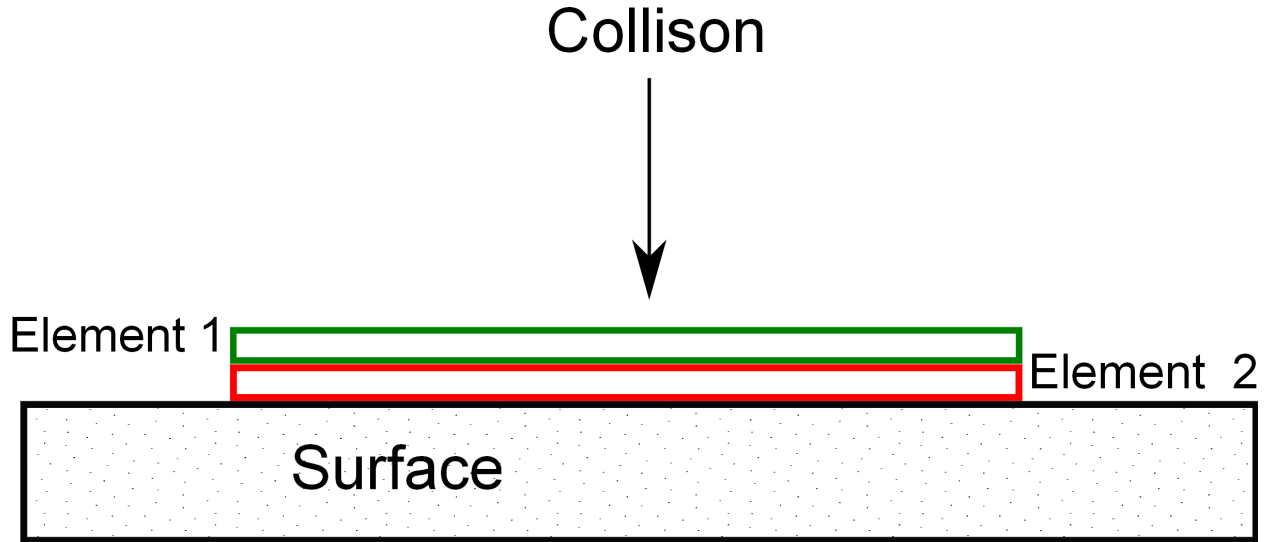
Figure 3.2: Pressure Sensor Construction Diagram

The presence of the contact area component means that smaller objects generate higher pressure for equal force, which can be problematic for large area sensors. The electrical displacement(D), shown in Equation (3.8), now depends on the pressure piezoelectric constant (d_{33}).

$$D = d_{33}S \tag{3.8}$$

The charge can be derived in a similar manner to the membrane approach, and the problem related to object size can be eliminated by making the sensor area sufficiently small such that the force is evenly applied over the area of the sensor resulting in the cancellation of the area terms. The canceling of the areas($A\&A_o$) yields a charge result(Q) directly proportional to the force(F) input, shown in Equation (3.9).

$$Q = d_{33}\frac{F}{A_o}A = d_{33}F \tag{3.9}$$

The construction eliminates the need for rigid mountings and free space of the membrane; however, the sensor output of strain due to pressure is much lower yielding more complex and specialized electronics. The pressure-based construction also requires a very rigid surface and/or substrate to generate pressure transduction.

3.5 Sensor Structure
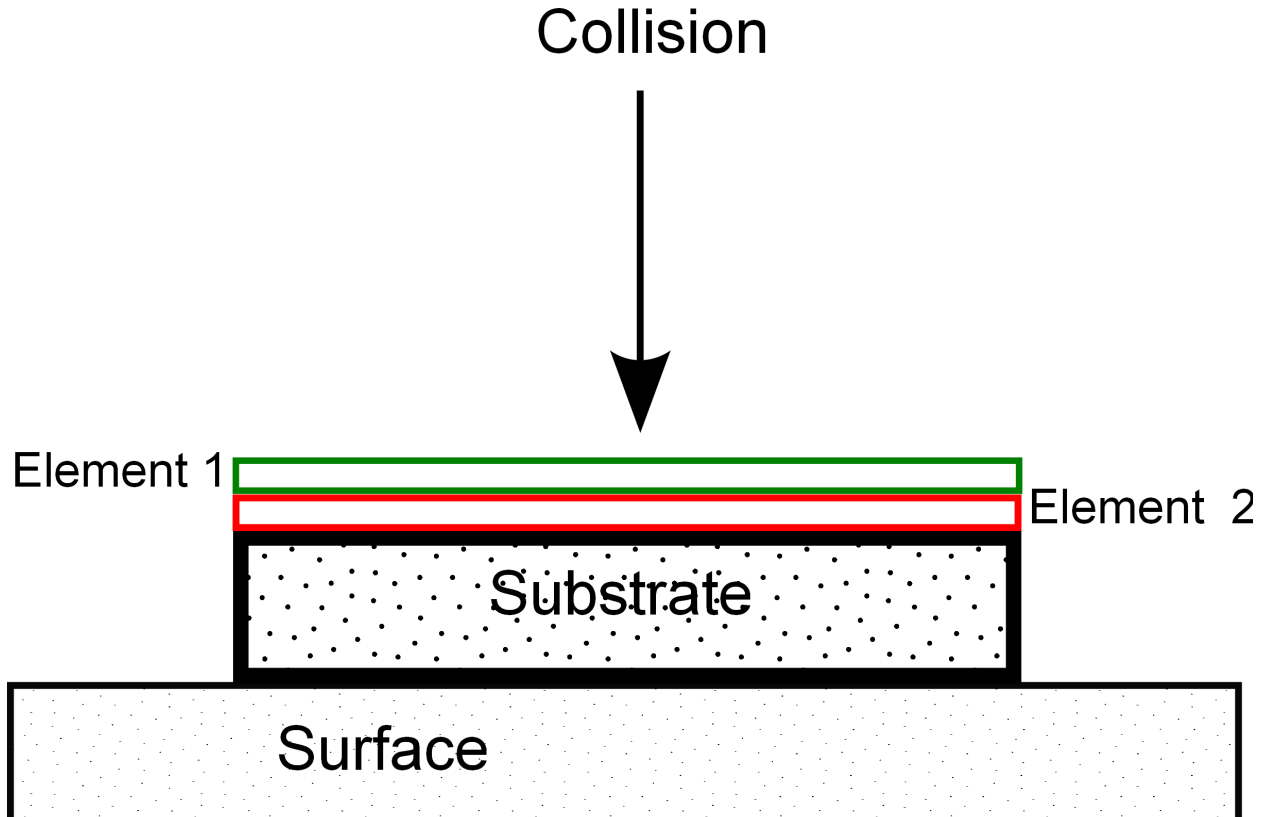
Figure 3.3: Pseudo-Membrane Sensor Construction Diagram

The collision sensor developed in the thesis is constructed from two PVDF film elements oriented with poles out of phase adhered to a flexible elastic compressible substrate. The trilayer sensor is attached to the targeted surface, shown in Figure 3.3. The construction yields a pseudo-membrane operation state in contrast to the traditional membrane and pressure-based design included as Figure 3.1 and 3.2, respectively and discussed in the previous sections . The collision stimulus deforms the elastic substrate due to localized compression and creates a resulting mechanical strain on the PVDF film elements that is mathematically related to the applied collision force in the next section. The elements act semi-membrane-like because the stress is an effect of the deflection due to compression. The elastic substrate should be chosen or designed to maximize the linear stress strain response

and also to minimize total sensor size for manufacturing and application concerns. The tri-layer pseudo-membrane approach using PVDF and an elastic substrate are capable of large area coverage because large PVDF sensing elements are easily constructed, the elastic substrate can be made of polyurethane foams and other commercially available compressible materials, and the sensor is not limited to planar surfaces because the pseudo-membrane approach creates stress from localized substrate compression and not film deflection as in a membrane approach. Recall the membrane based construction in Figure 3.1 required a certain amount of free space for deflection as well as rigid mountings. Also, recall the pressure construction in Figure 3.2 eliminated these issues but yields lower response and requires increased surface rigidity. The pseudo-membrane construction in Figure 3.3 eliminates the specialized construction requirements of rigid mountings for the membrane, free space for deflection, and rigidity of the surface affecting dynamic range. The dynamic range of the sensor and response are now controlled by the substrate material properties related to the thickness. However, the surface should be more rigid than the compressible substrate such that compression occurs, and the substrate should not be so hard or incompressible that the film elements begin to act in a pressure sensing capacity rather than membrane-like one due to deflection.

3.6 Response Modeling

For modeling purposes, the area of concern is restricted to the local frame of the collision. To maintain linearity of the response we will assume that the collisions will stay within the approximately linear region of the stress-strain response curve [25]. Also, the substrate will be treated as a continuum. The film stress from (3.2) is equal to the stress of the surface of the substrate, assuming a perfect adhesive bond and negligible effects of film sensor on substrate stress characteristics. For the reader's benefit, the material properties and modulus

20

utilized in the following response modeling are detailed and defined in Appendix A.

$$\underline{\boldsymbol{\sigma}} = \begin{bmatrix} T^{e1} \\ T^{e2} \\ T^{e3} \end{bmatrix} = \begin{bmatrix} \sigma_{11} & \sigma_{12} & \sigma_{13} \\ \sigma_{21} & \sigma_{22} & \sigma_{23} \\ \sigma_{31} & \sigma_{32} & \sigma_{33} \end{bmatrix} = \begin{bmatrix} \sigma_x & \tau_{xy} & \tau_{xz} \\ \tau_{yx} & \sigma_y & \tau_{yz} \\ \tau_{xz} & \tau_{yz} & \sigma_z \end{bmatrix} \tag{3.10}$$

By defining the Cauchy stress tensor $(\underline{\boldsymbol{\sigma}})$ of the substrate, (3.10), in terms of the normal and shear stresses, $\{\sigma_x, \sigma_y, \sigma_z\}$ and $\{\tau_{xy}, \tau_{xz}, \tau_{yz}\}$, X_{jk} in (3.2) can be replaced by the stress vector, T^{e3}, corresponding to the material surface resulting in Equation (3.11).

$$D = d_{31}(\tau_{xz} + \tau_{yz}) \tag{3.11}$$

Equation (3.11) shows the electrical displacement, D, as the piezoelectric constant corresponding to orthogonal stress multiplied by the combination of the shear stress in the length and width direction, τ_{xz} and τ_{yz}, respectively. From Equation (3.11), the stress contributing to the piezoelectric effect of the film is the orthogonal shear stress experienced by the substrate at the collision point. Therefore, the sensor dynamic range is dependent on the shear and normal stress characteristics of the chosen substrate. Using the shear modulus of elasticity (G) to relate shear strain to shear stress and Young's Modulus of the substrate (E) to relate normal strain to normal stress (3.12),

$$G = \frac{\tau_{xz}}{\gamma_{xz}} \qquad E = \frac{\sigma_z}{\epsilon_z} \tag{3.12}$$

along with the geometric representation of strain, (3.13),

$$\epsilon_{ij} = \frac{1}{2}(\frac{\delta_i}{j_o} + \frac{\delta_j}{i_o}) \tag{3.13}$$

and Cauchy's strain tensor ($\underline{\underline{\epsilon}}$) (3.14),

$$\underline{\underline{\epsilon}} = \begin{bmatrix} \epsilon_{11} & \epsilon_{12} & \epsilon_{13} \\ \epsilon_{21} & \epsilon_{22} & \epsilon_{23} \\ \epsilon_{31} & \epsilon_{32} & \epsilon_{33} \end{bmatrix} = \begin{bmatrix} \epsilon_x & \frac{\gamma_{xy}}{2} & \frac{\gamma_{xz}}{2} \\ \frac{\gamma_{yx}}{2} & \epsilon_y & \frac{\gamma_{yz}}{2} \\ \frac{\gamma_{xz}}{2} & \frac{\gamma_{zy}}{2} & \epsilon_z \end{bmatrix} \tag{3.14}$$

Assuming the substrate is under compression locally where $\delta_x = \delta_y = 0$, $\delta_z \neq 0$, and x_o, y_o are known static quantities, the shear stress is transformed to a compressive stress, using the relations (3.12) through (3.14). First, the shear stress of the film, τ, is transformed to the engineering shear strain, γ using the shear modulus of elasticity relation. The resulting engineering shear strains are equivalent to shear strains of the material because of the properties of the Engineering Strain Tensor outlined in Appendix A.2.

$$\tau_{xz} + \tau_{yz} = G(\gamma_{xz} + \gamma_{yz}) = G(2\epsilon_{xz} + 2\epsilon_{yz}) \tag{3.15}$$

Next, the shear strains are converted to geometric representations, and the fractions from Equation (3.13) cancel because of relations in the strain tensor (3.14). The resulting Equation (3.16) is now a function of the change in thickness, compression, of the material and the original dimensions–length and width.

$$\tau_{xz} + \tau_{yz} = G\left(\frac{\delta_z}{x_o} + \frac{\delta_z}{y_o}\right) \tag{3.16}$$

By combining the fractions and adding a term of the original thickness, the stress of the surface of the film is transformed to a proportionate function of the compressive strain of the material, ϵ_z, shown in Equation (3.17).

$$\tau_{xz} + \tau_{yz} = G\frac{z_o(y_o + x_o)}{x_o y_o}(\epsilon_z) \tag{3.17}$$

Finally, the compressive strain of the material is transformed from Equation (3.17) to compressive stress in Equation (3.18) such that the stress of the film, S, becomes a proportionate function of the compressive stress of the material caused by the collision of the object.

$$\tau_{xz} + \tau_{yz} = \frac{G}{E}\frac{z_o(y_o + x_o)}{x_o y_o}(\sigma_z) = S \tag{3.18}$$

In this case, compressive stress, σ_z, is a monotonically increasing and directly proportionate function of the force of the collision normal to the sensor where force towards the sensor produces a positive response. Specifically, higher levels of collision force should yields higher levels of compressive stress for the same object and lower levels of collision force resulting in lower levels of stress in the locally compressible area of the object in collision. By substituting the derived stress of the film sensor, S, into the piezoelectric electrical displacement formula from Equation (3.11) , the resulting sensor response is expressed in Equation (3.19)

$$D = d_{31}(\tau_{xz} + \tau_{yz}) = d_{31}\frac{G}{E}\frac{z_o(y_o + x_o)}{x_o y_o}(\sigma_z) = d_{31}(S) \tag{3.19}$$

Therefore for a measured stress S in Equation (3.19) and the electrical displacement of the pseudo-membrane sensor should also be a monotonically increasing function of the force. Modeling of strain was primarily accomplished with reference to [25].

3.7 Instrumentation

3.7.1 Amplifier Electronics

The electronics interface for the PVDF film elements requires high signal gain, low output impedance, high input impedance, low time constant to capture 1Hz collisions, and a minimization of the electric field effect of the sensor. A charge amplifier is used to minimize effects of sensor and line capacitance by minimizing input impedance, to minimize electric field by grounding sensor electrode, and because the sensing elements act as a current
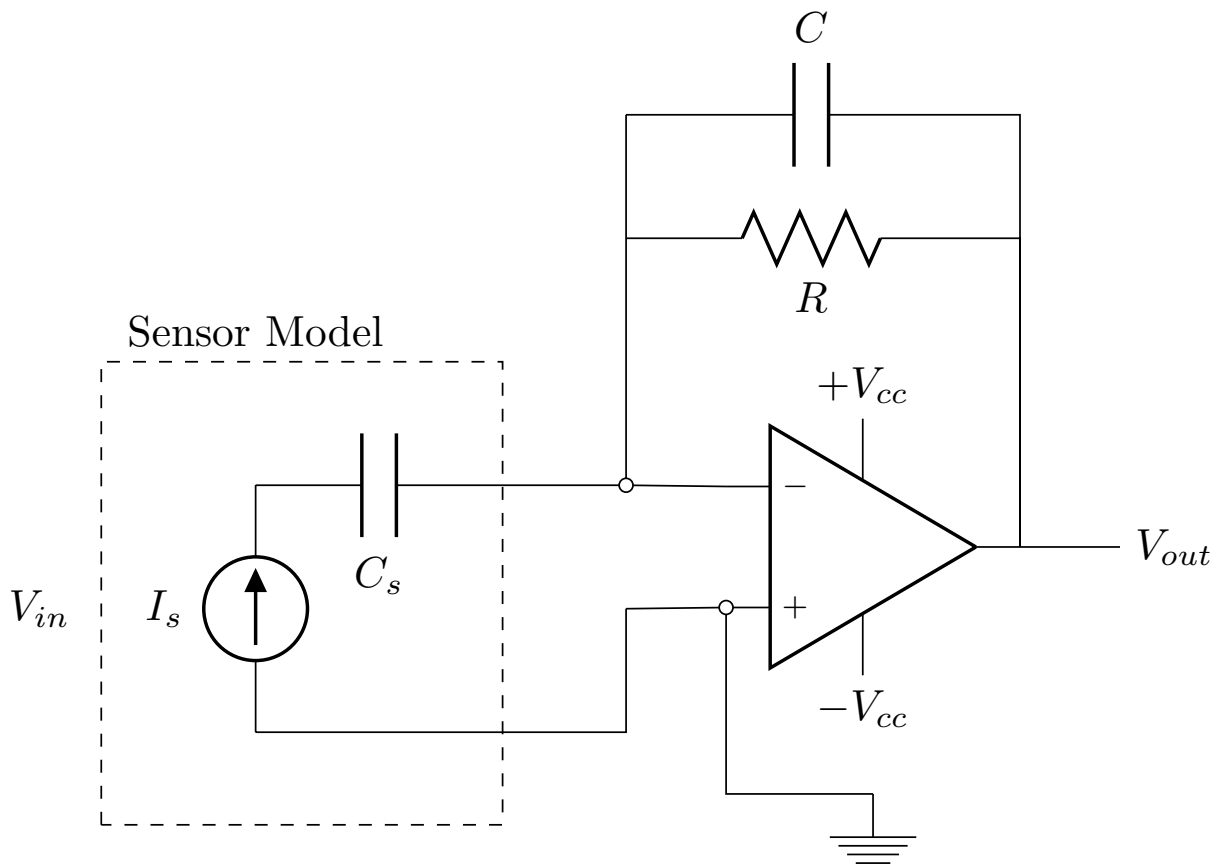
Figure 3.4: Charge Amplifier Circuit Design

source. The circuit, shown in Figure 3.4, acts as a single pole high-pass filter with a bleed resistor added in parallel to create a low enough cutoff frequency to properly detect physical interaction in the 1Hz - 1000Hz range [21]. The transfer function is shown in (3.20):

$$H(s) = \frac{V_{out}(s)}{V_{in}(s)} = \frac{sRC_s}{sRC + 1} \tag{3.20}$$

The system can be properly designed to yield a low enough corner frequency calculated from (3.21),

$$f_c = \frac{1}{2\pi RC} \tag{3.21}$$

which gives the needed low-end frequency range. The signal is then low-pass filtered with a cut-off frequency to attenuate unwanted signals and conditioned for input to the analog to

24

digital converter (ADC). The charge amplifier allows for positive and negative voltage range of +/- V_{cc} to create the large dynamic range needed for collision detection.

3.7.2 Sampling and Detection Electronics

The collision detection and sampling of the post amplified signal is performed in multiple ways. Threshold level collision detection is implemented utilizing a comparator and tunable reference voltage. The threshold voltage level is chosen based on signal response for desired collision force level. The comparator circuit works by outputting a "1" when the sensor signal exceeds the voltage threshold and then a "0" when the signal returns below. The circuitry is easily interfaced with solenoids or electronic interrupt hardware to create a stop function, satisfying industrial safety requirements [22]. Sub-threshold level collision detection is accomplished digitally by feeding the sensor signal into ADC's. The ADC inputs require signal conditioning to achieve full sensor dynamic range; specifically, the signal from the amplifiers should be rectified to the voltage range available to the ADC and then shifted such that all signal data is captured. The circuitry involves a passive voltage rectifier is implemented with resistors and an active voltage shifting circuit using a unity gain non-inverting operational amplifier and an offset reference voltage. The ADC converts the conditioned signal to digital values which can then be processed to detect collision events which occur below the threshold or sampled and sent back to a computer for data logging. For the experimentation and results detailed in the following chapters, the ADC and resulting digital values are used in the sampling format.

3.8 Design Attributes

The sensor design allows for complex planar and non-planar applications. The pseudo-membrane allows for high dynamic sensing range and applications while eliminating the construction requirements of membrane and pressure sensors. Recall that the membrane sensor construction requires free space for diaphragm deflection as well as rigid structures

for mounting the sensor element. The pseudo-membrane eliminates the need for free space by utilizing a locally compressible substrate and the rigid mounting is also not needed because adherence to the substrate creates mounting for sensor stress during deflection. Recall the pressure based construction eliminated free space needs, but required a highly-rigid substrate or surface to generate acceptable dynamic range. The pseudo-membrane maintains the ease of use of pressure actuation, but eliminates the high rigidity requirement because the sensor is acting in a deflection mode. The sensor design differs from state of the art tactile and collision sensing design in the following manner:

- high dynamic sensing range for collisions

- simple construction for ease of application to existing and future systems

- does not require rigid mountings or free space

- rigidity of surface is not a primary factor in response dynamics

- tactile shape and size is limited only by manufacturing technologies

- current technology allows for easily producible collision sensors based on the design and available parts

The experimental methods and results presented in the following chapters will expound upon published work on the sensor design by more accurately characterizing the force of the object during impact and additional statistical analysis on previous results [8]. The sensor design provides a novel collision sensing solution for complex robotics and automated systems where safety and system coverage are of higher concern than high resolution tactile perception.

Chapter 4

Experimentation Methods and Prototype

This chapter will outline the prototype sensor and electronics utilized in testing. Also, the experimentation methods used will be shown. The prototype sensor is constructed to represent a planar and non-planar application for the design. The electronics are detailed including the specified frequencies for amplifier design. The approximate force experimentation for collision simulation is detailed. Also, a more accurate force measurement method is presented utilizing high speed cameras and image correlation techniques.

4.1 Prototype Sensor

Initial prototype sensors for testing were constructed from poled 28 μm thick PVDF film elements, each 171 mm by 19 mm (length and width) and a 0.5 inch polystyrene closed cell foam substrate. The polyurethane foam was chosen for availability and to allow for large amounts of compression at collision. The trilayer sensor was constructed by adhering the two films, Element 1 and Element 2 from Figure 3.3, out of phase such that Element 1's top electrode is positive and Element 2's top electrode is negative, adhering the bilayer PVDF film to the polystyrene foam substrate and then affixed to the sample robotic arm shield for collision testing. The prototype sensor is shown in Figure 4.1 with curved portions and edges representing non-planar applications and the flat parts of the prototype representing planar applications.

4.2 Prototype Electronics

Signal capture was performed using previously described amplifier circuit design interfaced to 12-b analog to digital converters on an Atmel Xmega microcontroller using a buffer
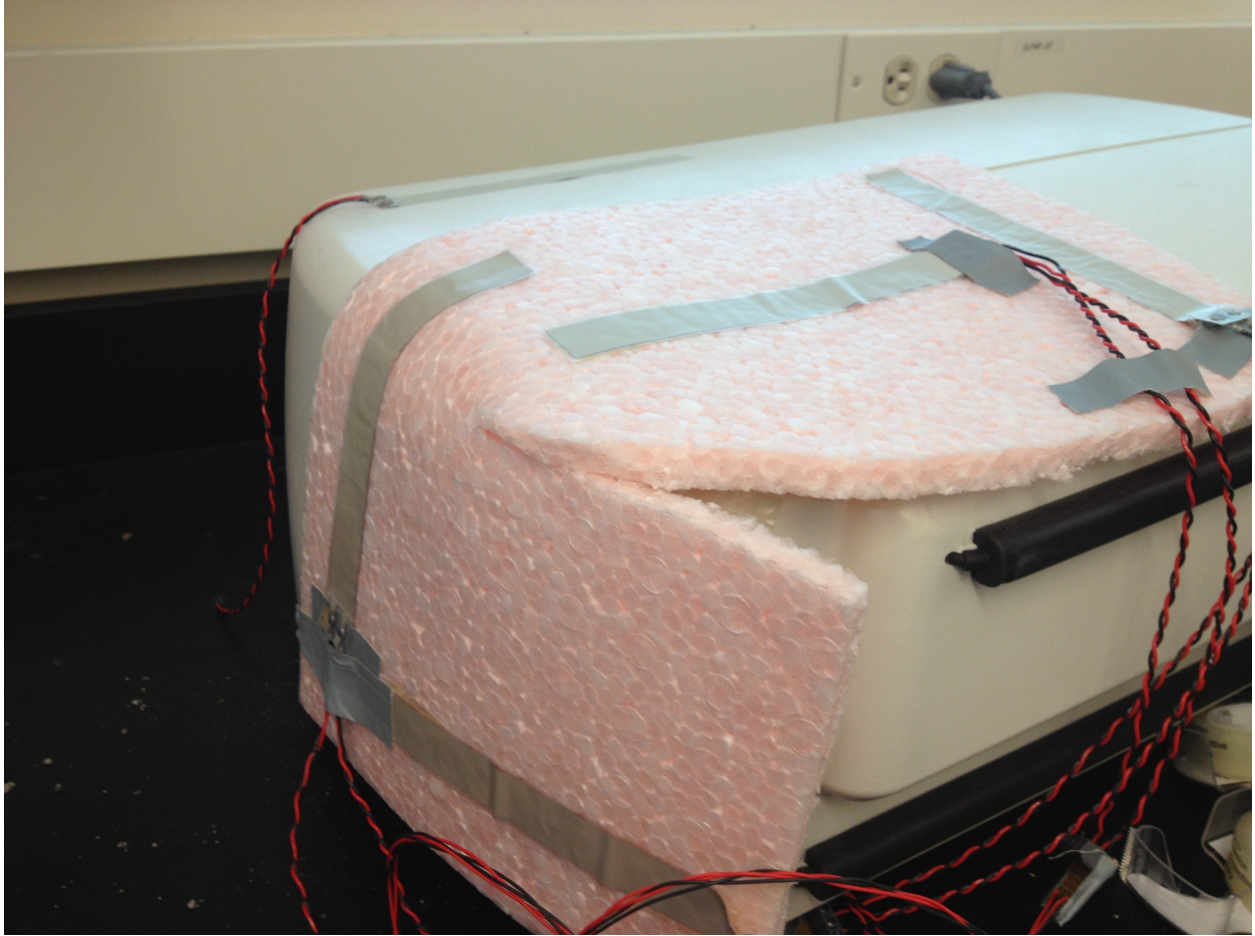
Figure 4.1: Sensor Prototype used in testing showing planar (top of cover) and non-planar (rounded left end) sensor applications on example robotic arm shielding. Wires in picture connect sensor electrodes to instrumentation.

and signal conditioning amplifier stage. The charge amplifier was designed with a $1.6\,\text{M}\Omega$ bleed resistor and $100\,\text{nF}$ charge accumulating capacitor yielding the following corner frequency:

$$f_c = \frac{1}{2\pi RC} = \frac{1}{2\pi(100\,\text{nF})(1.6\,\text{M}\Omega)} = 0.997\,\text{Hz} \tag{4.1}$$

which gives the needed low-end frequency range. The signal is then low-pass filtered with a $1\,\text{kHz}$ cut off frequency to attenuate unwanted signals. The charge amplifier allows for a positive and negative voltage range of $15\,\text{V}$ to $-15\,\text{V}$ to allow for high gain and large dynamic range. Because the ADC operates from $0\,\text{V}$ to $3\,\text{V}$, the signal output of the charge amplifier

28

is regulated down to the $-1.5\,\text{V}$ to $1.5\,\text{V}$ range and then shifted up $1.5\,\text{V}$. The ADC uses a reference voltage of $1.5\,\text{V}$ in differential mode resulting in a digital output range of -2048 to $+2048$ corresponding to a V_{LSB} of $7.32\,\text{mV}$. The ADC's sampling frequency is $93.7\,\text{kHz}$ which is more than 40 times the bandwidth of the analog input. Data was logged using serial communication with signals down-sampled to 10kHz.

4.3   Method

4.3.1   Collision Simulation and Approximate Force

Collision stimuli for testing was generated by dropping an object of known weight and uniform contact area on the sensor from varied heights to produce controlled impact collisions. Average Force of the object during impact (F) is approximated using the conservation of energy, shown in Equation (4.2), and the work-energy principle, shown in Equation (4.3), where distance to slow down (d) is compression of the substrate, defined as compressive strain multiplied by thickness.

$$mgh = \frac{1}{2}mv^2 \tag{4.2}$$

$$Work = F * d = \frac{1}{2}mv^2 = mgh \tag{4.3}$$

The work energy principle states that work is equal to the change in kinetic energy meaning that average impact force over the slow down distance is therefore equal to the original potential energy of the mass. The height(h) includes the slow down distance and height of object from the surface.

An approximation of distance for the object to slow down is a 50% compression of the substrate resulting in a slowdown distance of 0.25 inches. The approximate method allows for comparison of collision responses which closely simulate real world events; however, the approximate average force output has some inherent inaccuracy because of nonuniform compression of the material, variations of accelerations due to the non-uniformity over the range of collision stimuli, and bounce during impact. The average force due to work-energy

principle assumes the object is stopped in impact and does not account for non-zero velocity which occurs during rebound; therefore, the average force during impact is likely higher, especially for larger collisions where excessive bounce occurs. The method does not provide exact force estimation–particularly for the upper dynamic range of the sensor; however, he experimental method provides a good reference of response from smaller and larger levels of collision force to characterize the dynamic range of the sensor design and substrates; Table 4.1 shows the collision stimuli and approximate average force generated from the impacts. Objects used in testing were a Craftsmen wrench in size 15 mm and 22 mm, for types 1 and 2 respectively.

Table 4.1: Collision Stimuli

Data Set	Object Type	Weight	Object Height	Average Force
A	I	353 g	1.5 cm	5 N
B	I	353 g	3 cm	10 N
C	I	353 g	5 cm	20 N
D	I	353 g	8 cm	30 N
E	I	353 g	10.2 cm	40 N
F	II	597 g	10 cm	60 N
G	II	597 g	13 cm	80 N
H	II	597 g	16.3 cm	100 N
I	II	597 g	32.6 cm	200 N
J	II	597 g	49 cm	300 N

4.3.2 Force Measurement

For more accurate force representation of collision response, a secondary system is required to measure the displacement, velocity, and acceleration of the objects at impact to characterize the impacts. In order to limit the effects additional sensors would have on the physical dynamics of the model, object displacement, velocity, and acceleration measurement is performed using Digital Image Correlation (DIC) and a high speed camera. DIC is useful because of accuracy, computational efficiency, and elimination of the need to attach additional sensors [26]. The method utilizes a random spray or placement of particles as tracking points and correlates the movements of the points from image to image in order to

calculate the displacement from frame to frame. The measurement output for the system is the displacement of the object while in the frame of view of the camera. Acceleration is derived from the displacement by performing a line fit and taking the second derivative of the resulting polynomial. The collision stimuli for this force measured approach are presented in Table 4.2. The set is intended to mimic the coverage of the previous data set, and the presented average forces cover the range for the approximated method shown in Table 4.1.

Table 4.2: Collision Stimuli for Displacement Measurement Tests

Data Set	Weight	Object Height	Average Force
A	500 g	5 cm	38.58 N
B	500 g	10 cm	77.17 N
C	500 g	15 cm	115.75 N
D	500 g	20 cm	154.33 N
E	500 g	35 cm	270.08 N
F	500 g	50 cm	385.83 N

The testing setup utilizes a precision machined cylindrical weight with a rounded end in order to prevent sensor damage. The weight is machined to within 0.1 g of 500 g to simplify force calculations. The test setup is pictured in Figure 4.2.

The testing methods are designed to mimic real world impact collisions spanning the desired operating range of the sensor. The approximate method provides for efficient testing to confirm the planar and non-planar applications of the sensor. The presented force measurement method provides additional impact information of the objects during collision to support the results of the approximate method as well as characterize the impact characteristics of the foam. The prototype sensor represents the planar and non-planar applications for testing.
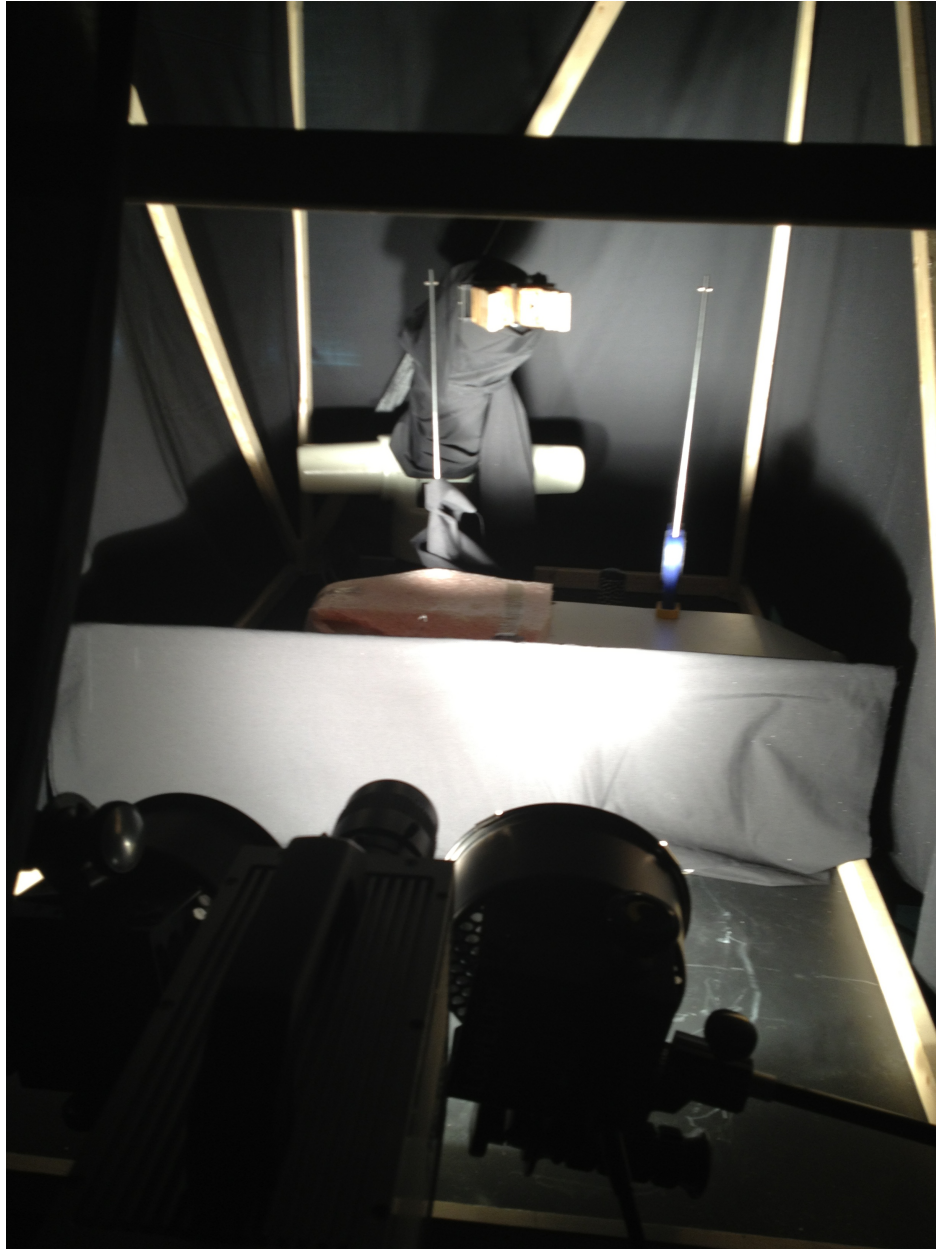
Figure 4.2: Experimental setup using High-speed(10000 fps) camera and robotic arm to create and measure consistent collision stimuli. The robotic arm is located over the sensor prototype which is clamped to the table to provide rigidity and is shielded from the heat of the lights by the illuminated wall in the front. The camera is behind the two 1000 W lights used to increase the contrast ratio of the falling object. The entire setup is contained in a light box environment to eliminate external interference.

Chapter 5

Results

This chapter presents and analyzes the results of the experimentation methods presented in the previous chapter. The results for the approximate force method show the sensor response to the range of collision stimuli described in Subsection 4.2.1 and shown in Table 4.1. For this result set, a planar sensor prototype and non-planar sensor prototype are tested, and the resulting responses are compared. Experimentation results from the force measurement method are presented for a planar case. The data set presented covers a similar collision range to the approximate method and has been previously provided in Table 4.2.

5.1 Average Force Experimentation Method

Recall from Subsection 4.3.1, the experimentation utilizing average force is carried out by generating multiple collision stimuli from the heights specified in Table 4.1. The multiple collision tests are performed on both planar and non-planar sensor prototypes, and the resulting signals are captured. The mean response of both sensor prototypes is taken, and the peak of the mean response is utilized in comparison. Statistical analysis is also performed on the resulting peak measurements to characterize the sensor response to varying levels of collision force for both sensor prototypes.

5.1.1 Planar Sensor Prototype

The sampled mean results, presented in Figure 5.1, show the wide dynamic sensor range, from $5\,\mathrm{N}$ to $300\,\mathrm{N}$, and consistent response to collision. The mean response for each collision force level is shown on the graph. The sensor response is the value of S derived from the

measured electrical displacement, previously shown in Equation (3.19). Recall the planar sensor prototype is the flat area of the example cover previously shown in Figure 4.1.
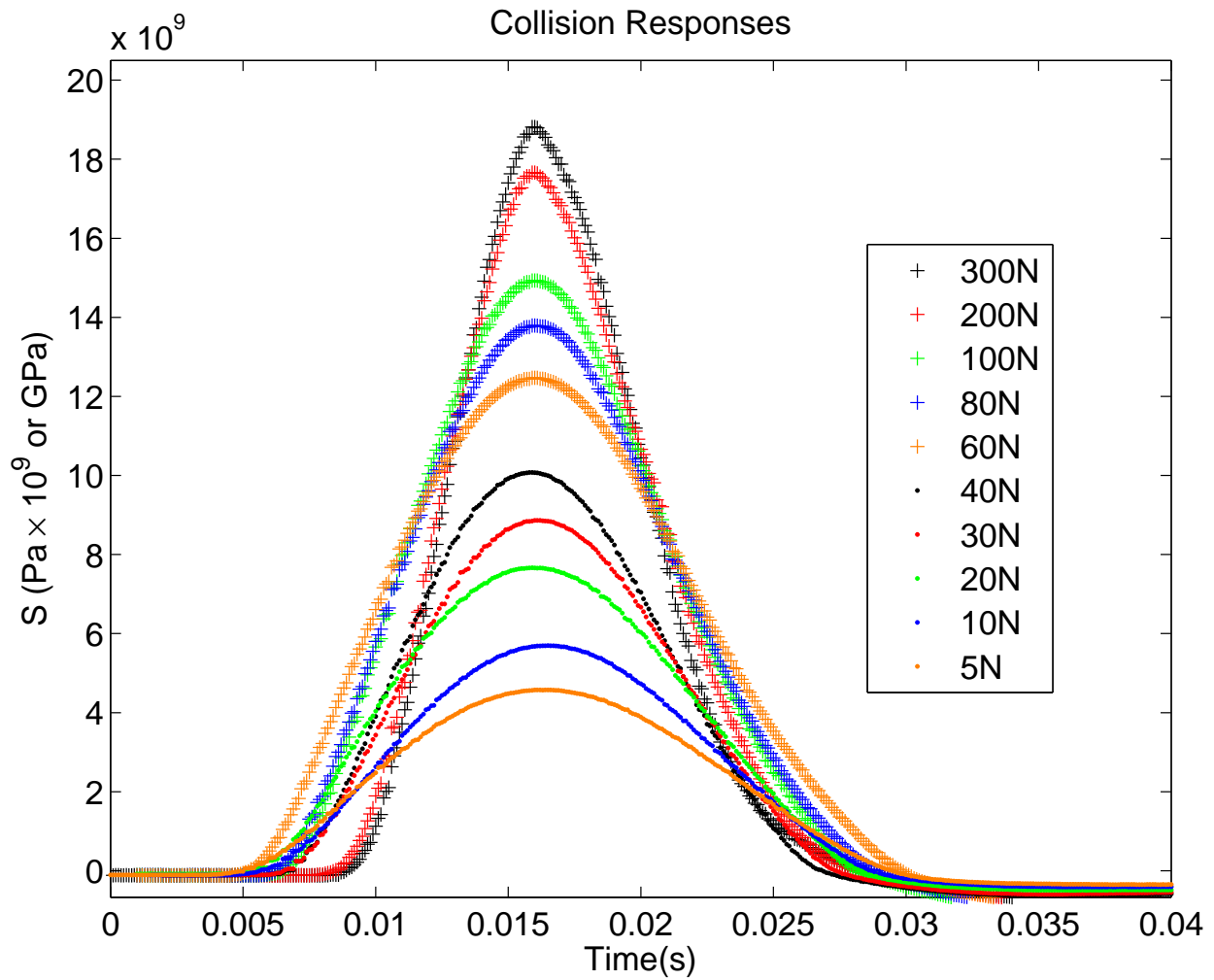

Figure 5.1: Mean captured results for wide dynamic range of collision stimuli for planar application of sensor.

The relation of applied collision stimuli to measured stress peaks resulted in Figure 5.2 showing that the sensor response is not totally linear. The relation resembles the engineering stress strain curves of polyurethane foam under impact, which reinforces the previous assertion that stress measured by the sensor is related to the localized compressive strain at the impact point [27].
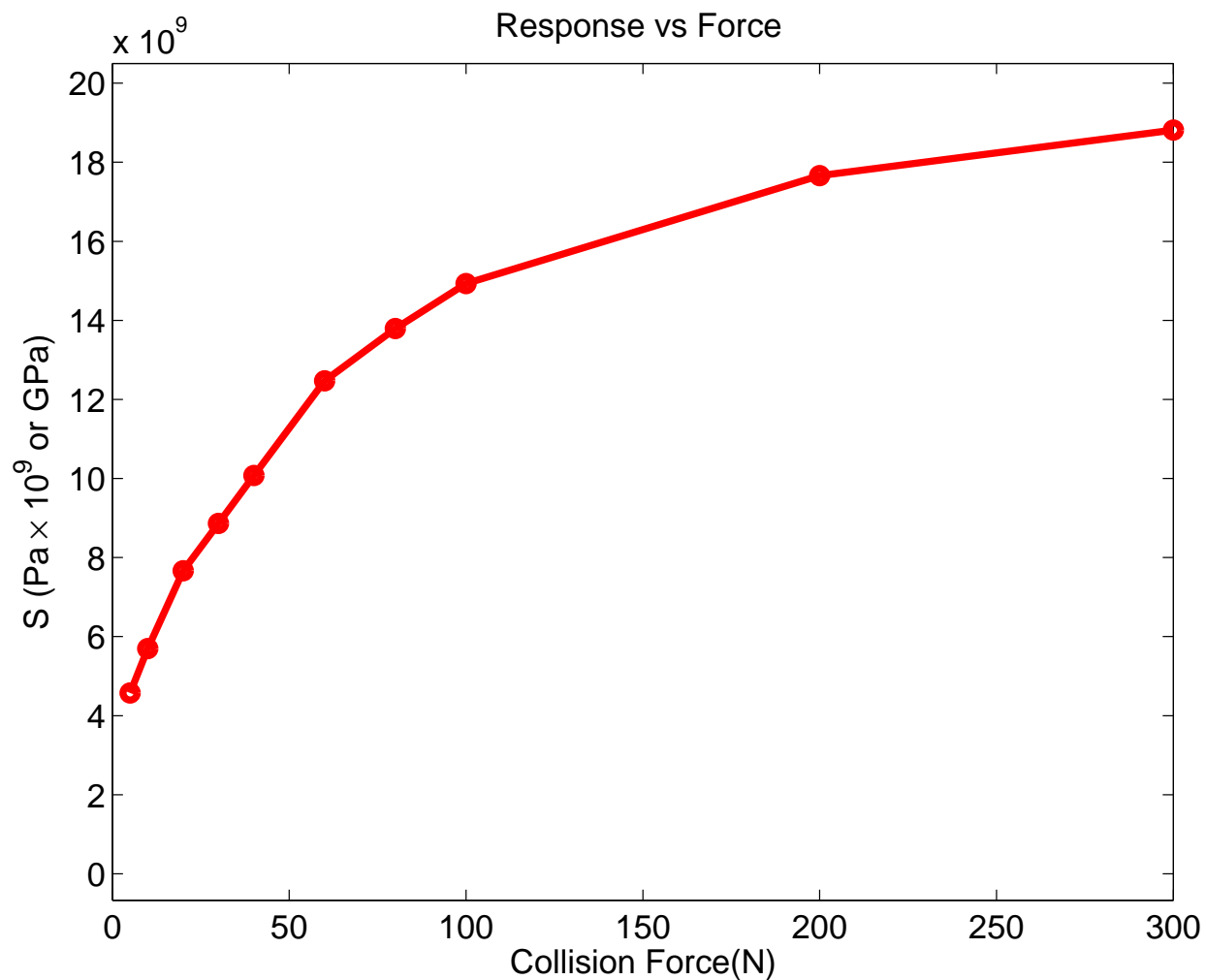
Figure 5.2: The relation of measured collision to approximate force of object collision for planar application shows an initial linear trend of high sensitivity but reaches a non-linear region and eventual plateau of decreasing strain experience and reduced sensitivity for force greater than 100N.

5.1.2 Non-planar Sensor Prototype

The results in Figure 5.3 show that the measured response from collision for a non-planar application strongly correlate with the results from planar application. Recall the non-planar sensor prototype is the curved end of the example cover previously shown in Figure 4.1. Some deviation is expected, but the sensor provides detection over the desired dynamic range for the non-planar application. The consistency between planar and non-planar experiments demonstrates the robust application properties of the sensor. The relation of measured system response to approximate collision force, shown in Figure 5.4, is also very similar to the graph from the planar testing exhibiting an initial linear region and then plateau.
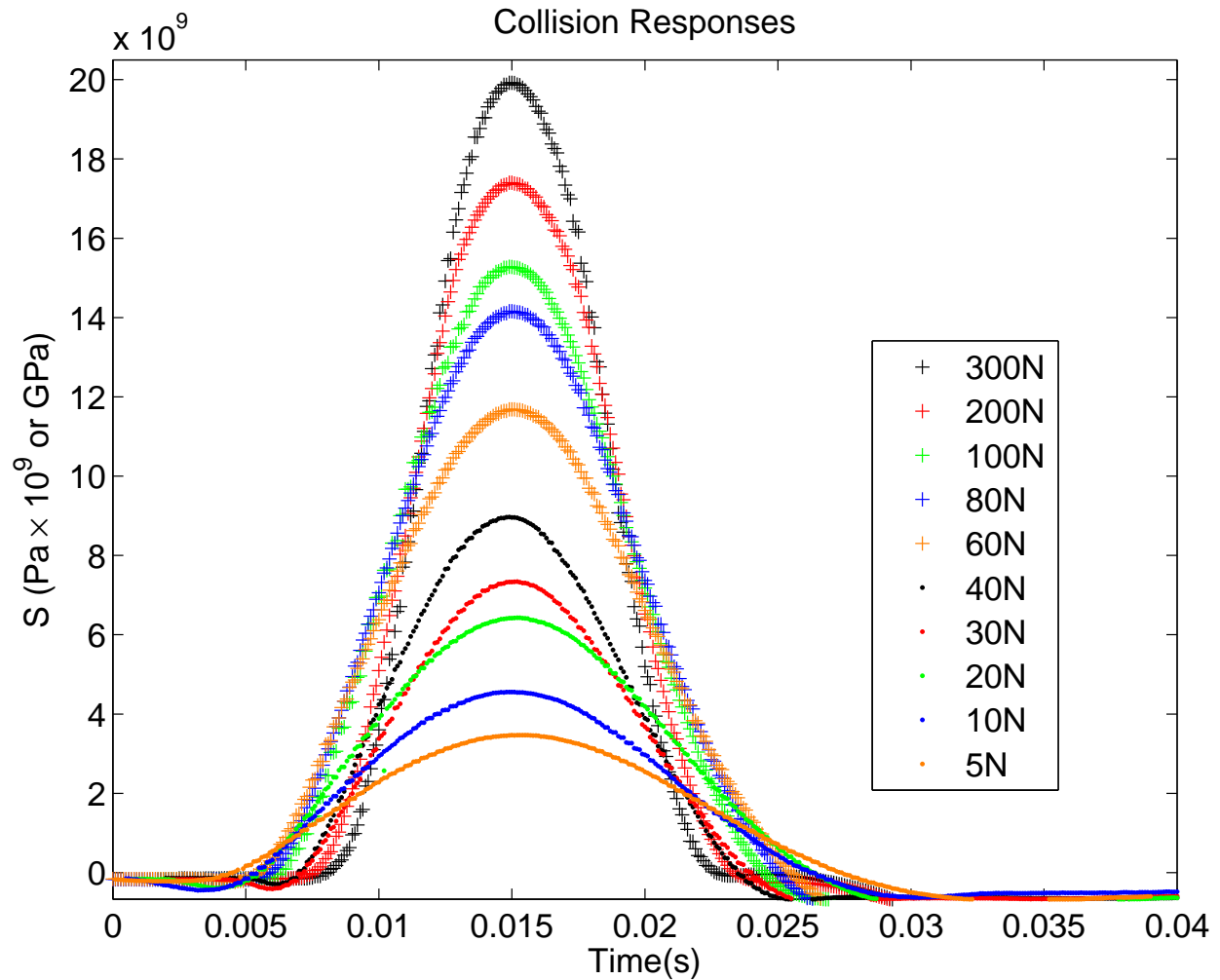
Figure 5.3: Mean captured results for wide dynamic range of collision stimuli.
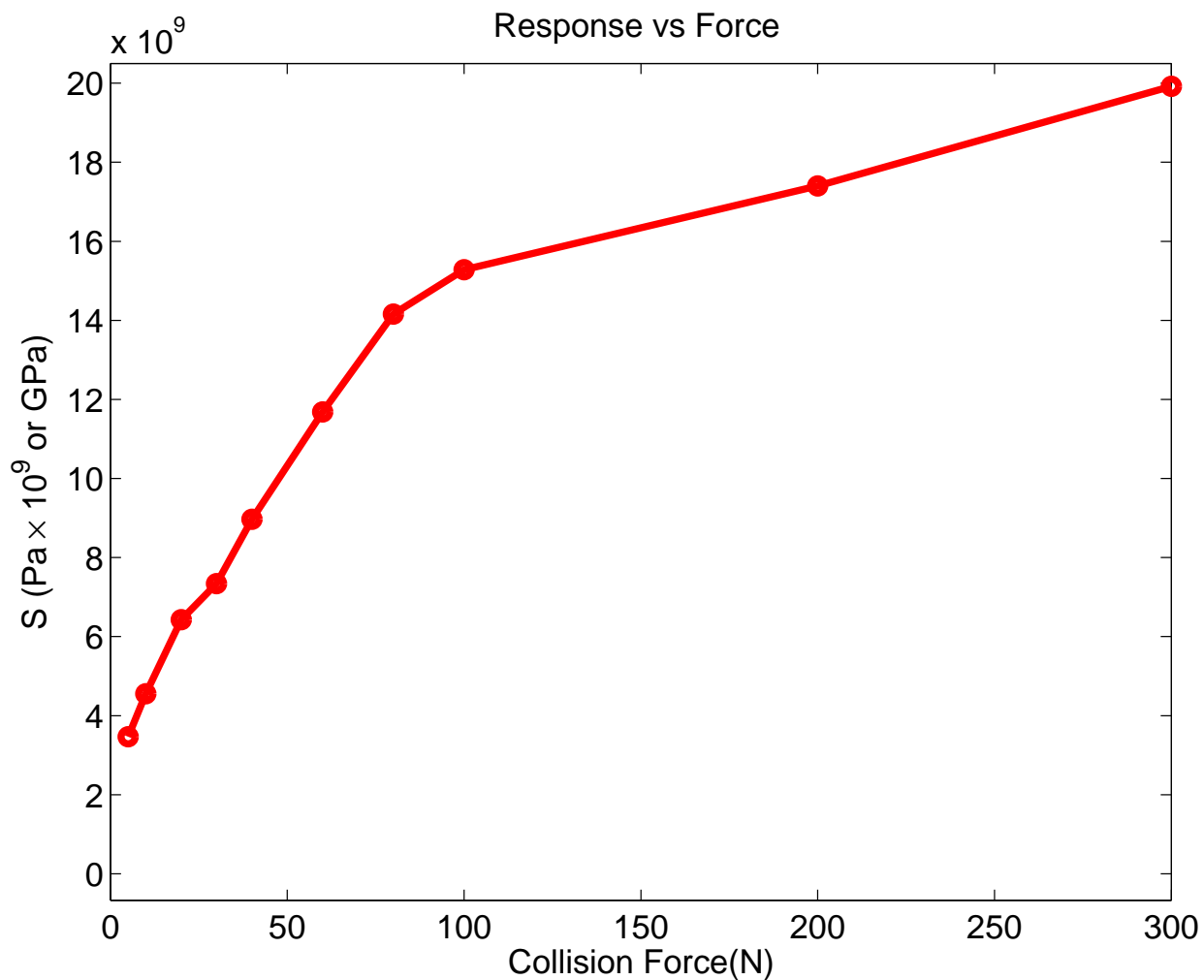
Figure 5.4: The relation of measured collision to force of object collision for sensor mounted on a non-planar surface shows an initial linear trend of high sensitivity but reaches a non-linear region and eventual plateau of decreasing strain experience and reduced sensitivity for force greater than 100N, very similar to the response graph of the planar application.

5.1.3 Low Force Dynamic Response

Figure 5.5 shows that there is little delay or difference in stress measured by the upper and lower sensors; however, some difference can occur because of de-lamination of the sensor elements from each other after repeated impacts with inadequate construction. Figure 5.5 also shows the uniformity of sensor response for the top and bottom sensor elements. The level of the digital response for the low impact should make it clear to the reader that low levels of collision are highly detectable by the sensor. The 5 N collision force of the impact generated a digitally quantized value in excess of 200, which represents the amplitude of the analog sensor signal. The quantized voltage has a least significant bit equivalent value of $1 = 7.32\,\text{mV}$.
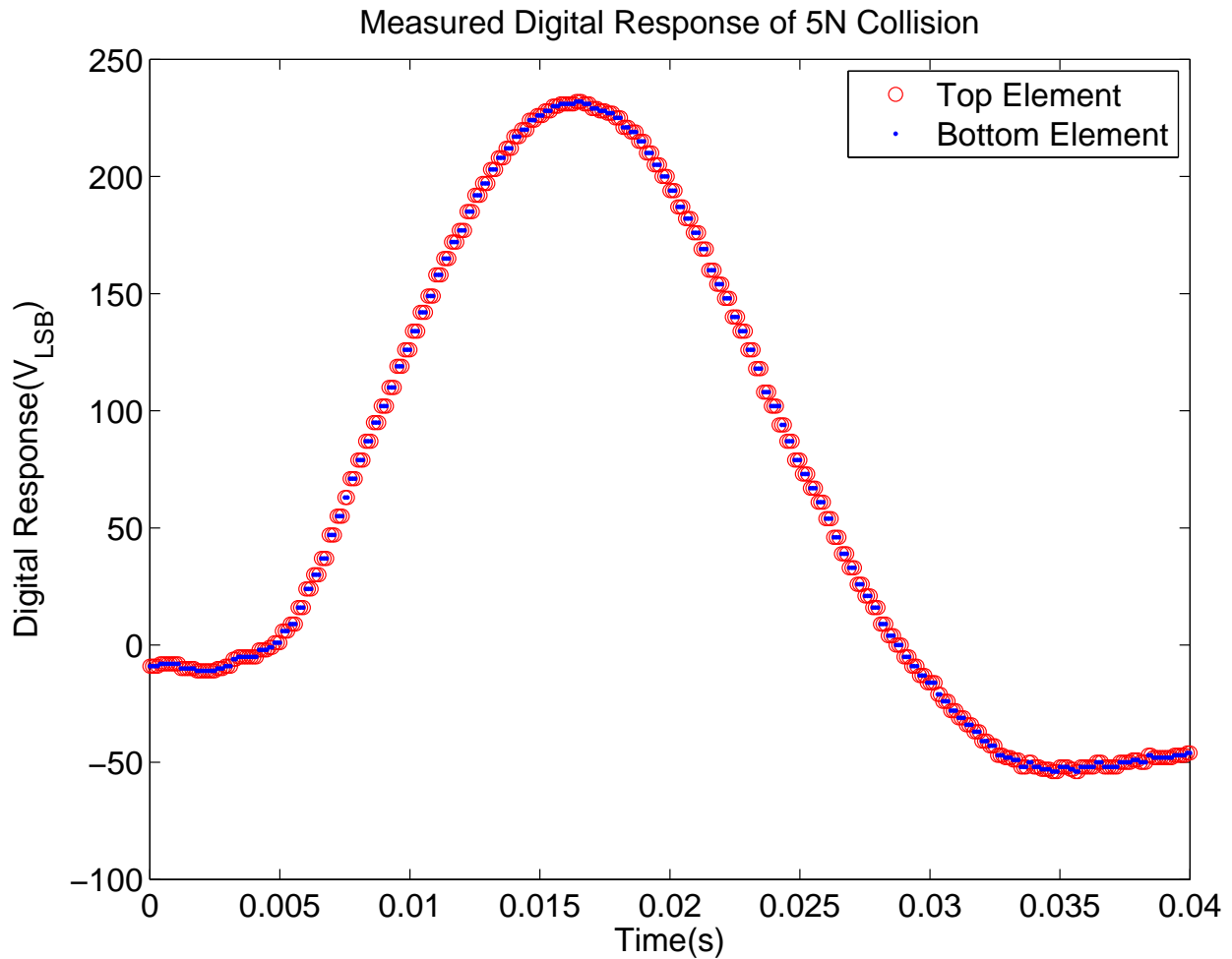

Figure 5.5: Mean Digital Response results of Element 1 and Element 2 for 5N collisions.

5.1.4 Total Results Comparison and Statistical Analysis

The complete data set values are compiled and shown in Table 5.1. The mean peak of the sensor response for planar and non-planar sensor prototypes have similar magnitude for each object drop height. The standard deviation for the planar sensor measurements exhibits the strong correlation and response density such that results between different force levels can be accurately distinguished. The higher levels of deviation in non-planar sensor response is likely resultant of some non-normal force during impact with the curved sensor application. The average standard deviation for the range of collisions levels for planar sensor prototype is 0.4079 GPa. The non-planar results, which exhibit the previously discussed deviations, have an average standard deviation of 0.7098 GPa. The compiled results show the preciseness of the sensor response for planar and non-planar applications. However, additional force measurements are necessary to accurately model the object impacts and sensor response, given in the following section.

Table 5.1: Total result comparison of planar and non-planar sensors with mean, μ, and standard deviation, s, for each force stimuli set.

Data	Height	Force	μ_p (GPa)	s_p (GPa)	μ_{np} (GPa)	s_{np} (GPa).
A	1.5 cm	5 N	4.576	0.267	3.466	0.441
B	3 cm	10 N	5.695	0.265	4.557	0.794
C	5 cm	20 N	7.664	0.362	6.427	0.656
D	8 cm	30 N	8.864	0.422	7.339	0.676
E	10.2 cm	40 N	10.078	0.395	8.970	0.762
F	10 cm	60 N	12.470	0.413	11.686	1.010
G	13 cm	80 N	13.792	0.392	14.157	0.667
H	16.3 cm	100 N	14.392	0.556	15.284	0.669
I	32.6 cm	200 N	17.663	0.520	17.400	0.864
J	49 cm	300 N	18.814	0.487	19.923	0.559

5.2   Force Characterized Collision Response Method

In this section, the falling object is tracked utilizing a 10000 frame-per-second camera, and the displacement is derived from the videos utilizing the image processing method described in Subsection 4.3.2. The displacement measurement for the object falling, impacting the sensor, and then rebounding is shown in Figure 5.6. Figure 5.6 shows measurements for a 5 cm drop and the different phases of the object movement are highlighted.
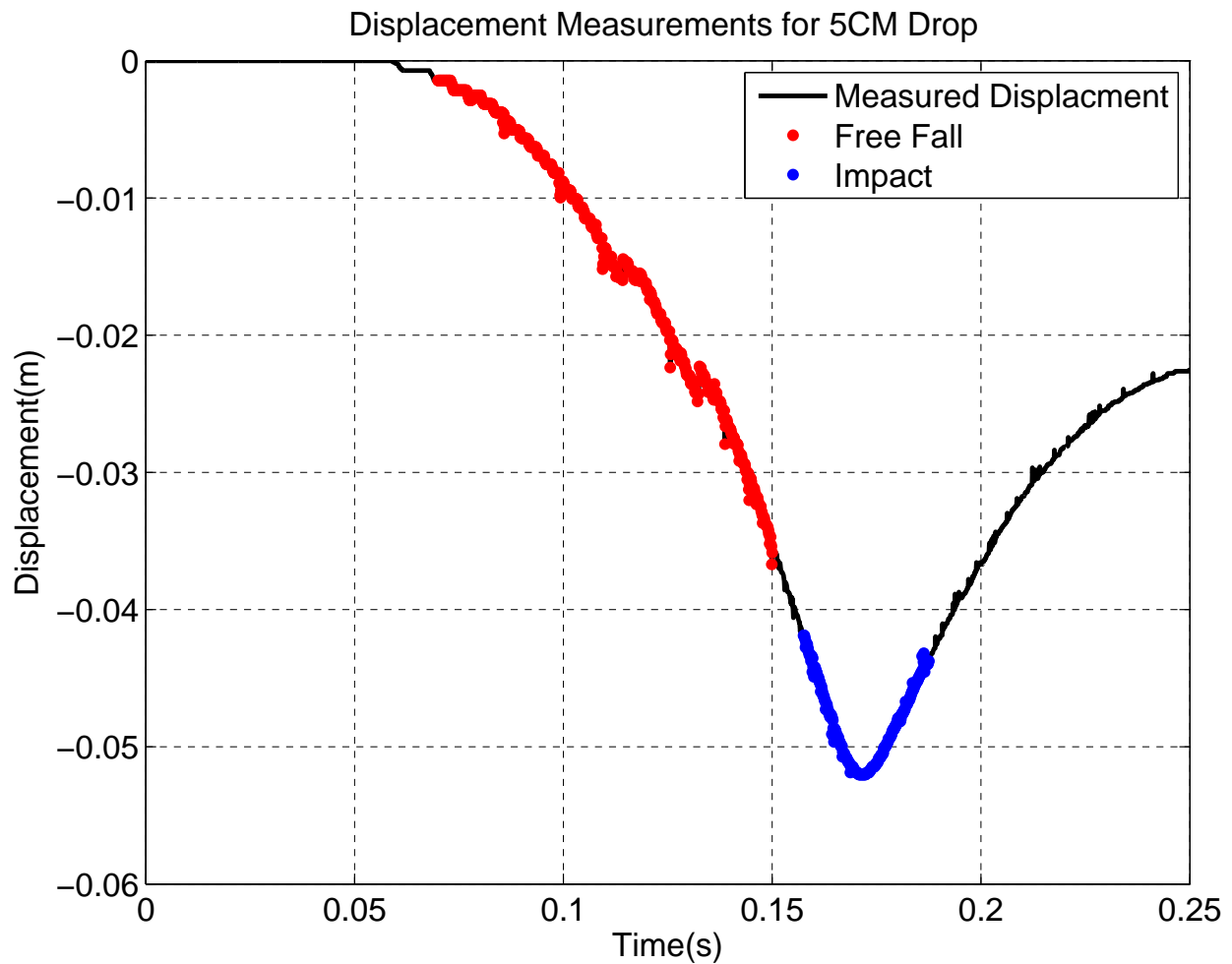

Figure 5.6:   Measured displacement for 5 cm drop. The displacement measurements corresponding the object in free fall and impact are highlighted in red and blue respectively.

The free fall portion, highlighted in red, is utilized to confirm measurement validity by estimating acceleration due to gravity, which is detailed in Subsection 5.2.1. The portion of importance for collision force measurement–the impact period–is highlighted in blue. The displacement measurement during this impact region is used to calculate the accelerations of the object during impact, and using the mass of the object, the resulting peak impact force is derived. The method for force calculations from displacement measurements is detailed in Subsection 5.2.2.

5.2.1 Gravity Confirmation

In order to verify the method of displacement and force measurement, the object movement is captured in free fall prior to impact. Using the free fall displacement window, the acceleration due to gravity is achieved by a second order line fit to the displacement measurements and sample validity is determined. Over the range of collision stimuli specified in Table 4.2, the estimated gravity during free fall has a root-mean-square error of $0.275\,79\,\mathrm{m/s^2}$ and mean value of $-9.7815\,\mathrm{m/s^2}$ The gravity measurements are shown in Figure 5.7.

5.2.2 Force Measurement

The force of the object during collision is calculated from the measured displacement during the impact of the object. The line fit of the displacement data is utilized in a similar fashion to the gravity confirmation method; however, the polynomial line fit is of higher order and the primary concern is the peak response. The relation of measured peak response for the data sets to the height of the object dropped is shown in Figure 5.8. The measured force response to height follows a monotonically increasing trend. The force levels shown in Figure 5.8 do not achieve the levels of strain to clearly show the plateau of realizable force which will occur at higher levels of impact. The results show that peak force impact is higher than estimated average impact from Table 4.2, as expected, because object rebound is not compensated for in the average impact force derivations in Equation 4.3.
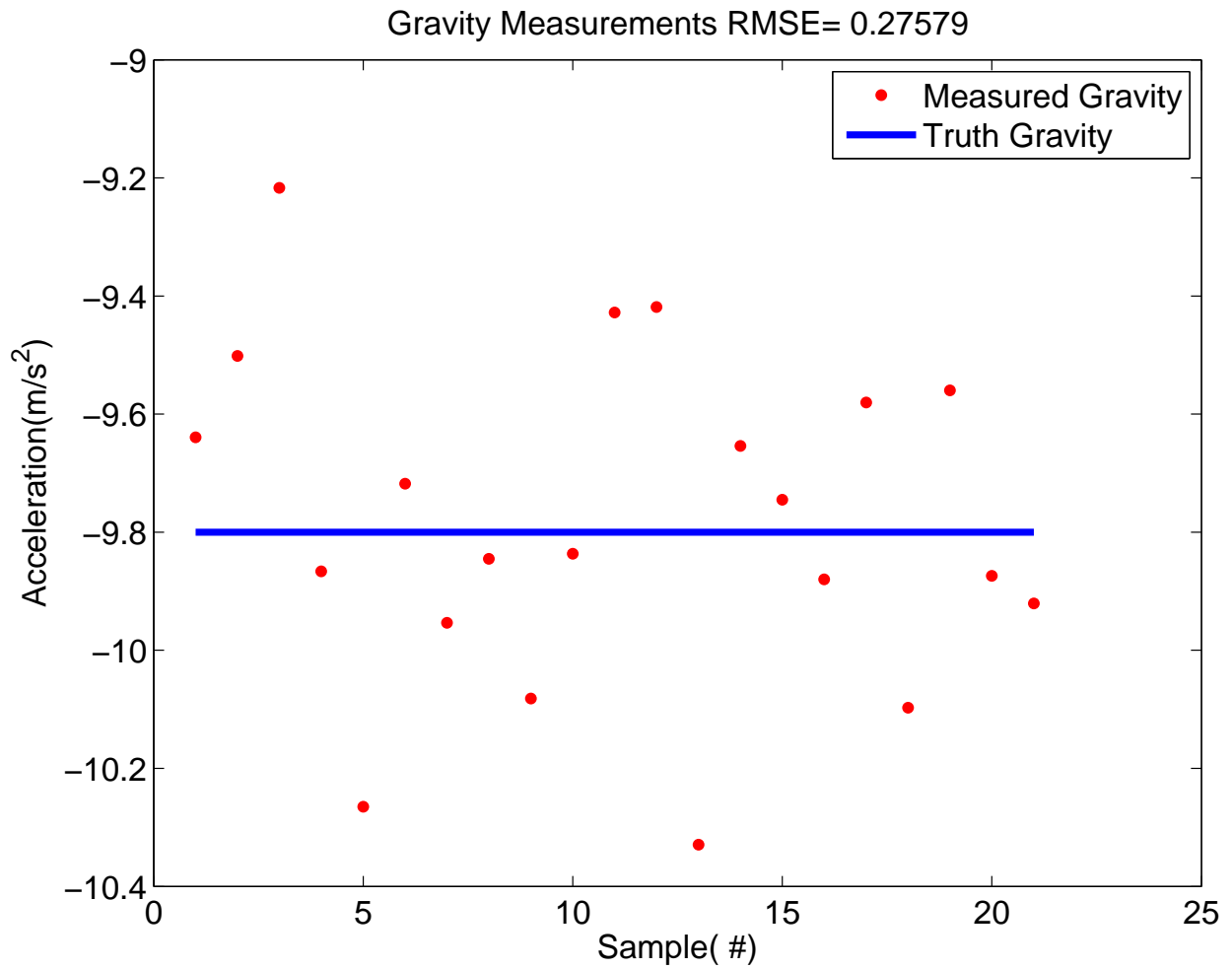
41

Figure 5.7:   Gravity measurements made to confirm validity of displacement measurements with a root-mean-square error of $0.275\,79\,\mathrm{m/s^2}$ and mean value of $-9.7815\,\mathrm{m/s^2}$.
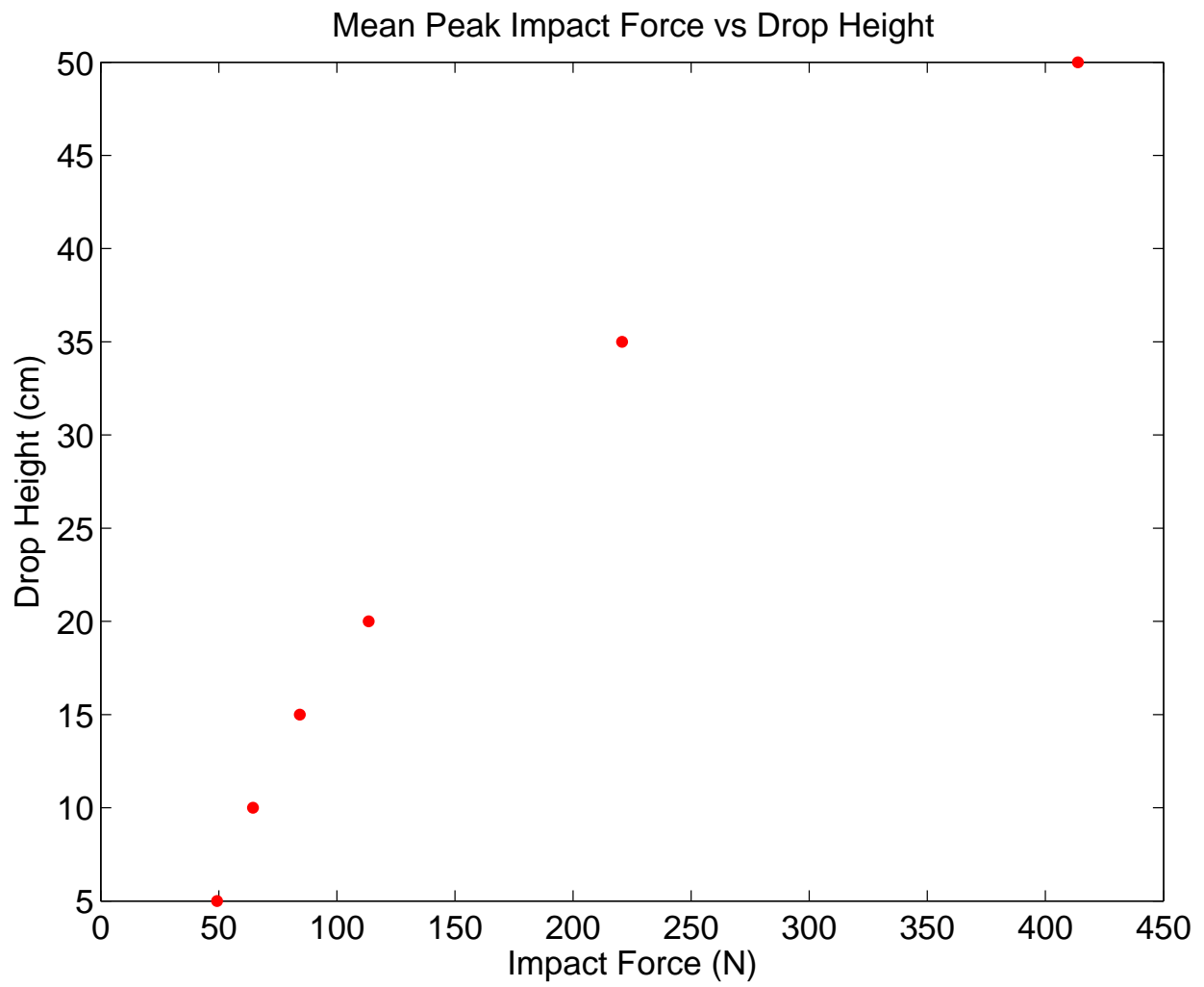
Figure 5.8: Mean of measured peak impact force for drop height of object during collision stimulus.

5.2.3 Sensor Response

The sensor response for the object impacts for each data set were captured in order to characterize the response to measured peak impact force. The sensor response resulting from the 5 cm object drop are shown in Figure 5.9. The measured values is the S component previously discussed in Equation (3.19). The sensor response shows strong uniformity and correlation for multiple impacts and a close grouping of peak response level. The sensor responses for 10 cm, 15 cm, and 20 cm object drop heights are shown in Figure 5.10 , 5.11, and 5.12 respectively.

Figure 5.9:   Measured sensor response for 5 cm drop with responses labeled by data run notation of [N9 Date Run#].

Figure 5.10:   Sensor response for 10 cm drop with responses labeled by data run notation of [N9 Date Run#].

The sensor response for heights ranging 5 cm to 20 cm all show similar uniformity and peak point grouping. The sensor responses in Figure 5.11 and 5.12 exhibit exceptional uniformity and tight grouping for peak sensor response. The deviation present in other responses is likely a result of object impact not being perfectly centered on the film sensor.
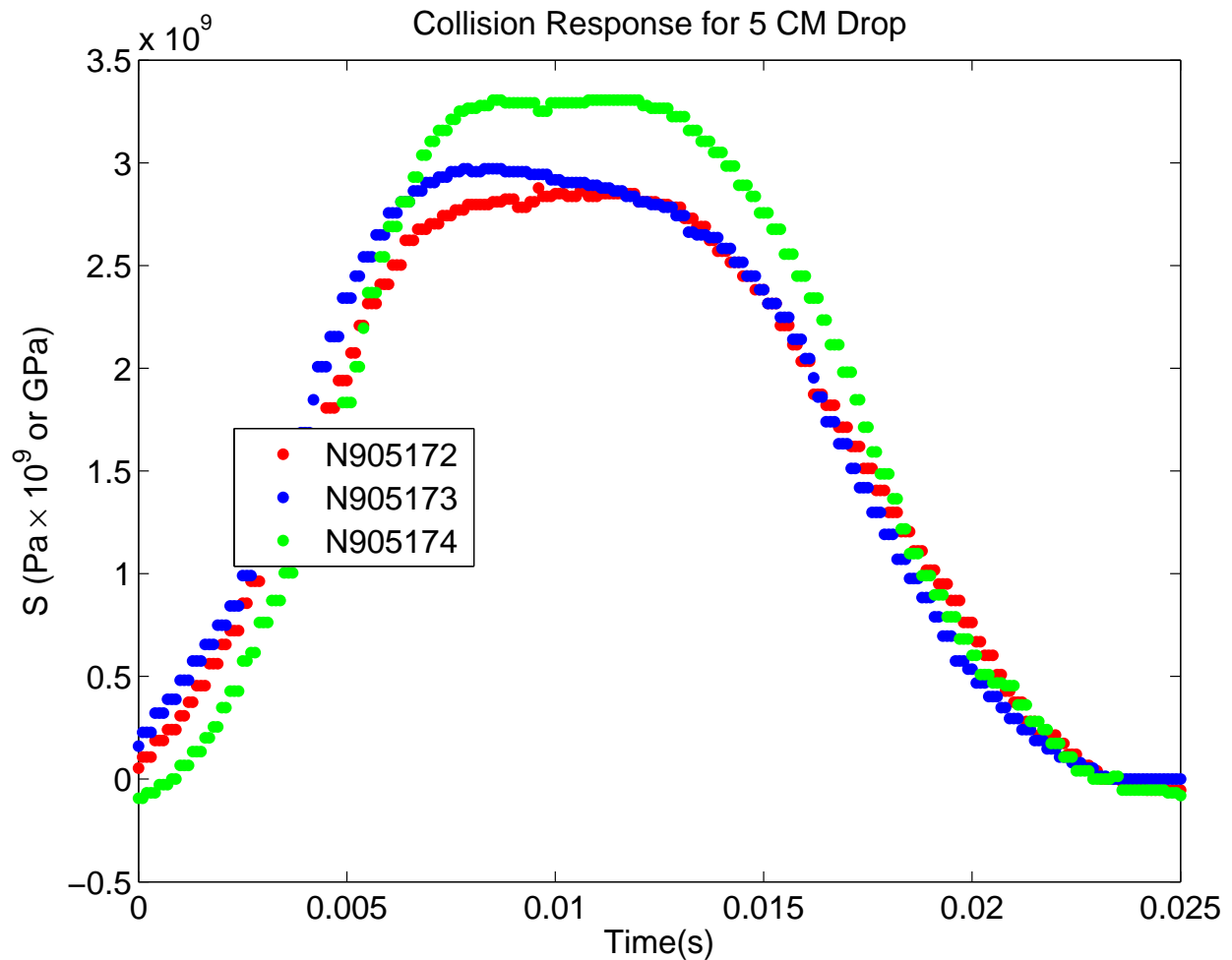
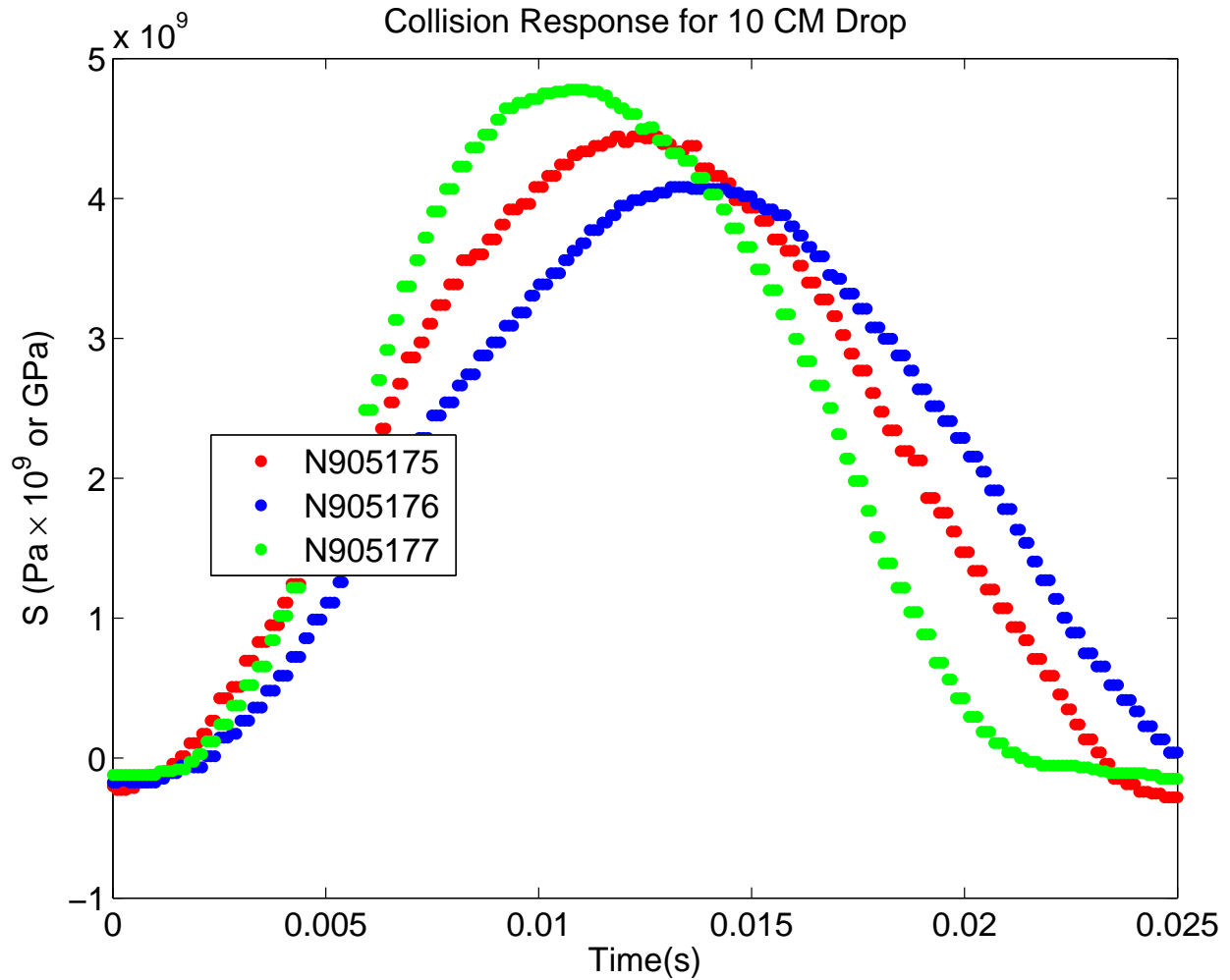Figure 5.11: Sensor response for 15 cm drop with responses labeled by data run notation of [N9 Date Run#].
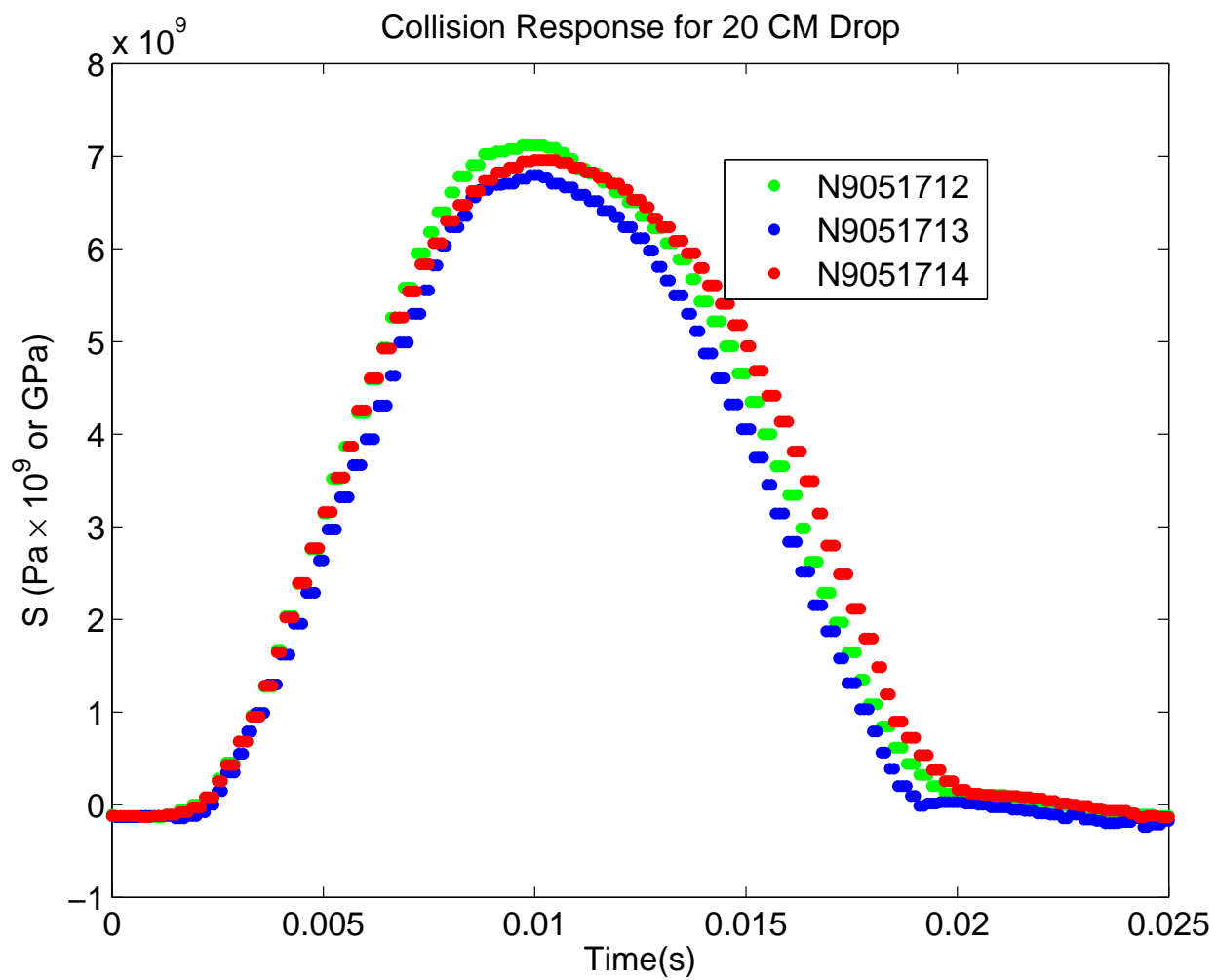
Figure 5.12: Sensor Response for 20 cm drop with responses labeled by data run notation of [N9 Date Run#].

The measured response corresponding to object impacts created from 35 cm and 50 cm heights exhibit the previously discussed deviation from object impacts not squarely colliding with the sensor. The low response in Figure 5.13 can be excluded from response mean calculations because it is clearly an outlier resulting from the object not cleanly impacting the sensor. The high dynamics of impacts for the object at the higher drop heights and force levels create deviation in the sensor response.
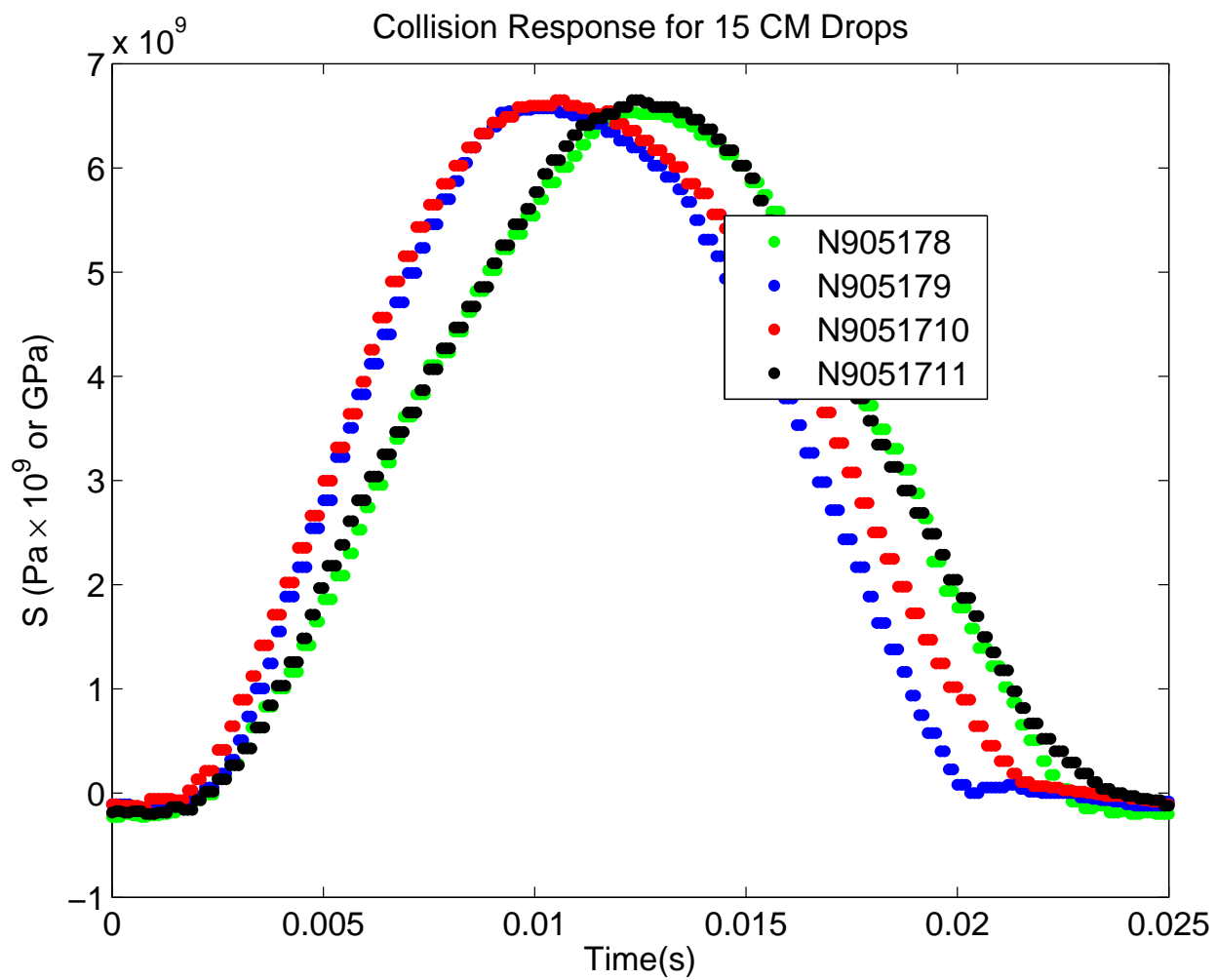

Figure 5.13: Sensor response for 35 cm drop with responses labeled by data run notation of [N9 Date Run#].

The responses for 50 cm drops, shown in Figure 5.14, show extreme deviation such that an accurate mean cannot be determined. However, the measured peak force for the higher levels of dropping does not exhibit the same amount of deviation. It is likely that variation in impact point between the object and sensor are the root cause of deviation for similar levels of measured force. The force measurements do not deviate because the foam substrate generates the same amount of response both on and off of the sensing tactile.
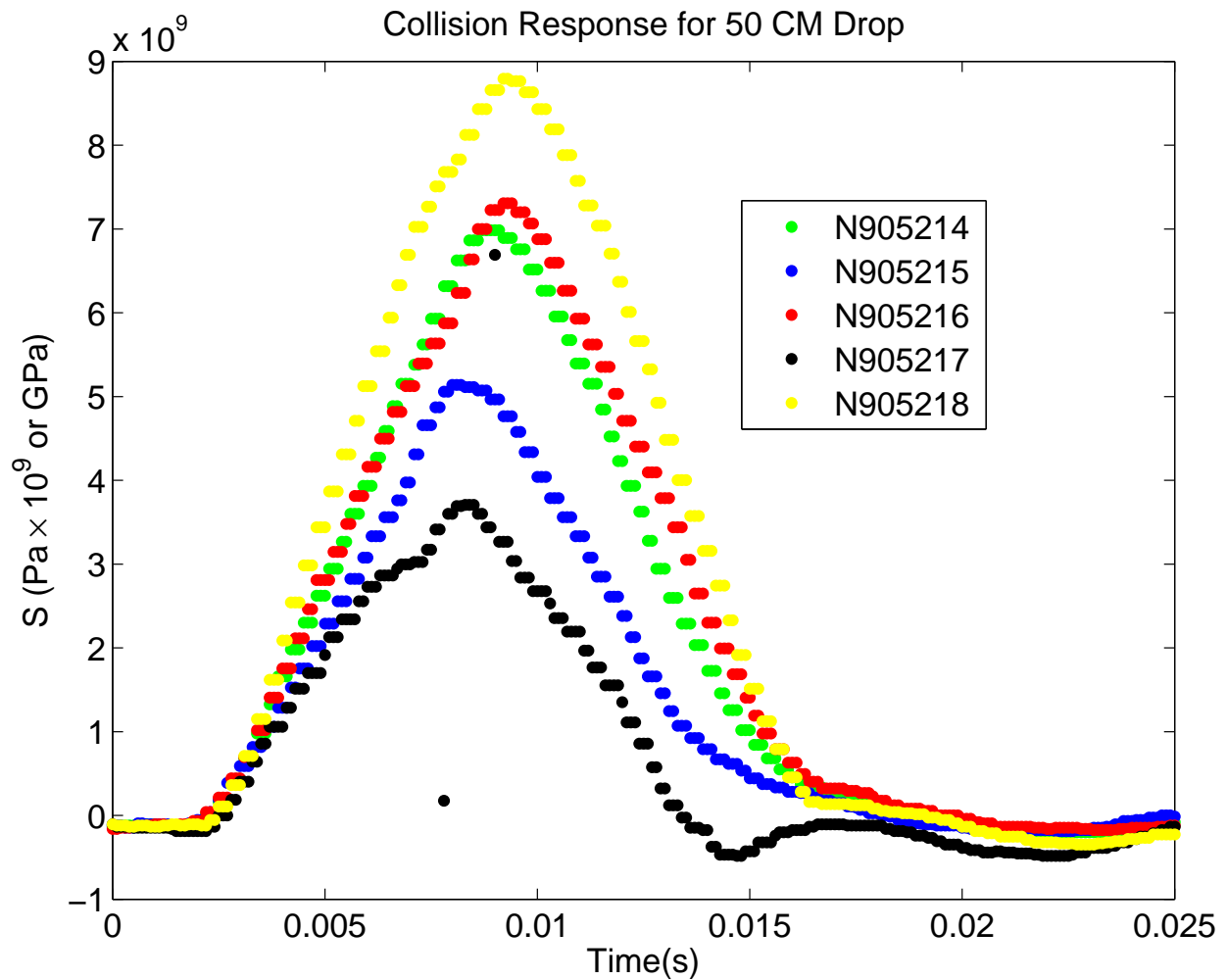
Figure 5.14: Sensor response for 50 cm drop with responses labeled by data run notation of [N9 Date Run#]. The data runs show extreme deviation because of object impacts partially impacting the tactile.
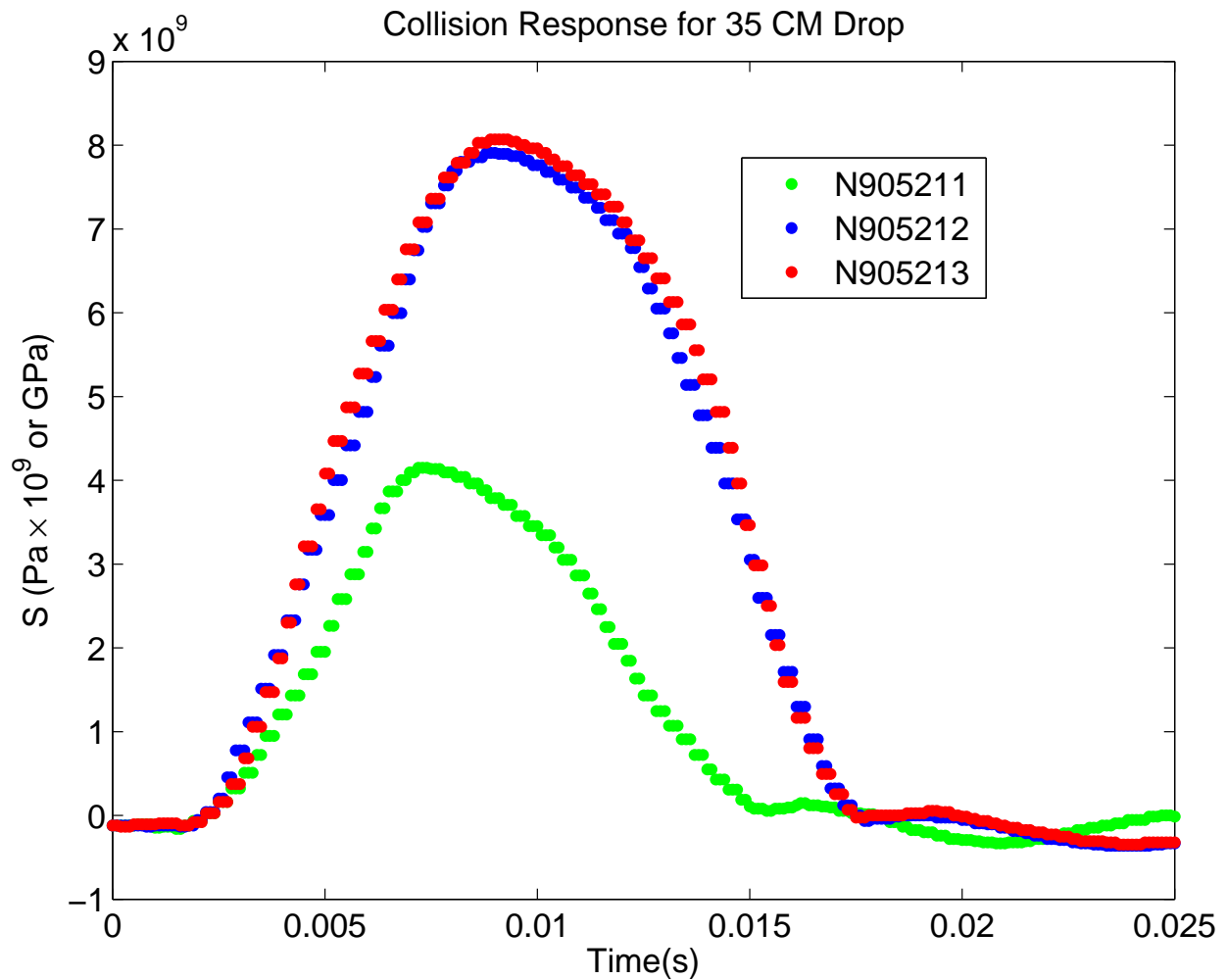
The measured sensor response for the range of collision detections, shown in Figure 5.15, shows the strong correlation of some sensor response levels while others exhibit more deviation. Unlike the average force experimentation method where large numbers of collisions were created (more than 30) for each level, the complexity of camera based displacement measurement and processing limited the number of achievable collisions. The low number of data points causes problems for sensor response measurement when the object does not squarely strike the sensor, as previously discussed.

Figure 5.15: Sensor response vs measured impact force for total data run including mean value line.

The trend of sensor response versus measured peak impact force strongly supports the previous results achieved using the approximate force method. The measured force detection of 49.315 N for the 5 cm shows the sensor is capable of low levels of collision detection down to 49.315 N. The detection at 413.778 N, while slightly inaccurate, clearly demonstrates the wide dynamic range of the sensor design.
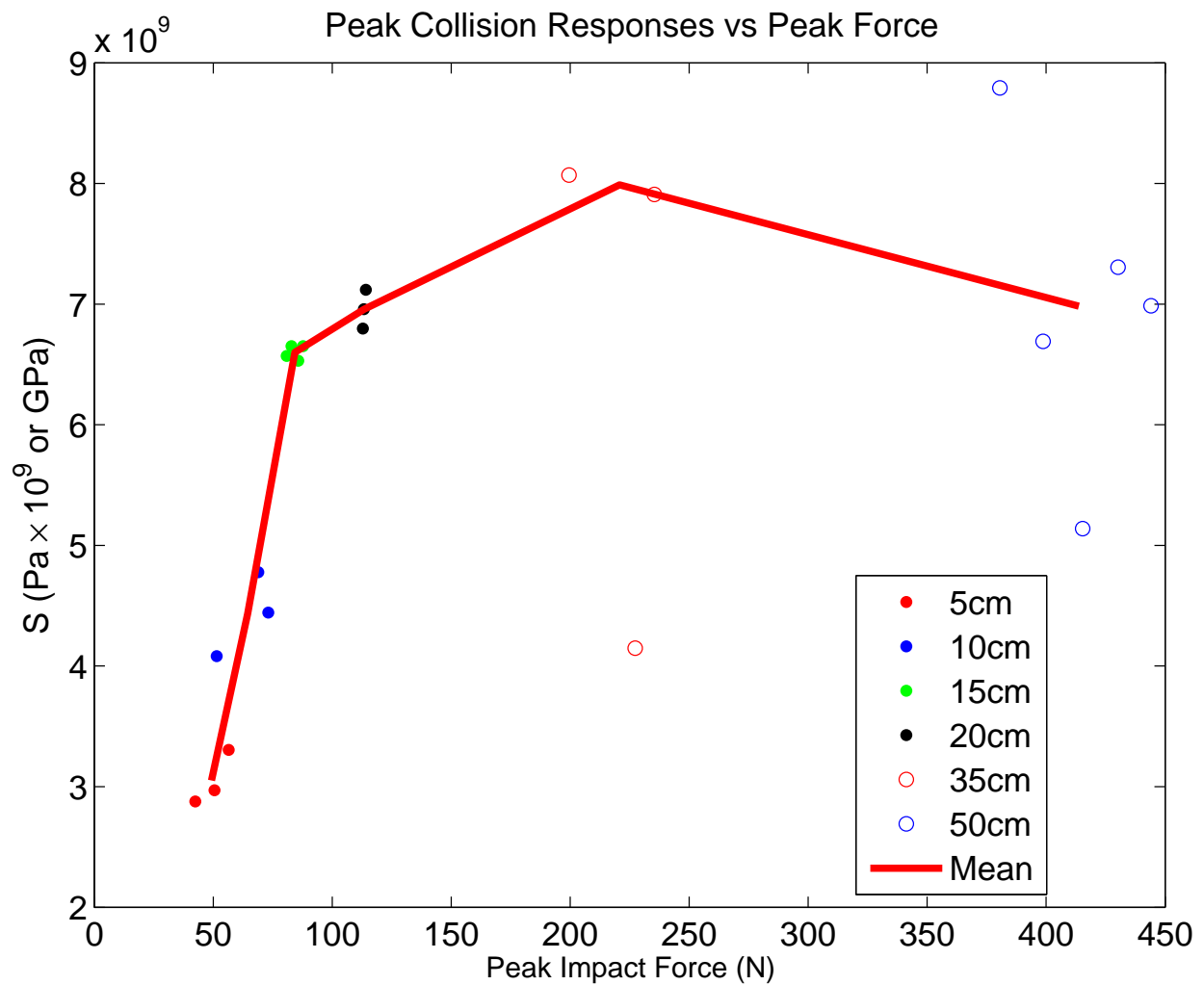
The results of collision response and force measurement are numerically represented in Table 5.2. The calculated mean of each collision level as well as sensor response are shown. The range of collision measurement and response is utilized in lieu of standard deviation calculations because of the low number of data points. The measured sensor response and impact force for the previously emphasized tightly grouped sets, corresponding to 15 cm and 20 cm, have significantly lower ranges of value than the other measurements. The tight grouping of sensor response and force measurement is likely because the impacts consist of primarily normal components of force, which is the case when the object falls straight down and impacts the sensor at a 90 degree angle. The results of the force characterized collision response method represent a similar result to the previous approximate force method. The relations show sensor response to be a monotonically increasing function of the impact or collision force of the object. Therefore, the sensor response supports the assertions and modeling present in Section 3.6 and achieves collision detection for a wide range of impact forces and applications.

Table 5.2: Total result comparison of measured sensor response and impact force object collisions for range of drop heights. The values in parenthesis for the 35 cm sensor response are the values including the outliers. The force measurements did not exhibit outliers.

Data	Height	μ_{Force} (N)	Range (N)	μ_{sens} (GPa)	Range (GPa)
A	5 cm	49.315 N	14.0956 N	3.0511	0.4282
B	10 cm	64.524 N	21.7028 N	4.4339	0.6959
C	15 cm	84.309 N	6.9066 N	6.6007	0.1204
D	20 cm	113.452 N	1.3143 N	6.9587	0.3212
E	35 cm	220.728 N	35.9005 N	7.9891(6.7089)	0.1606(3.9209)
F	50 cm	413.778 N	63.4738 N	6.9828	3.6533

Chapter 6

Conclusion

In contrast to existing technologies, the detailed sensor design developed in this thesis shows strong collision sensation for both planar and non-planar surfaces. The pseudo-membrane construction eliminates not only mechanical issues associated with pressure and membrane based sensation but also increases applicability of the PVDF sensing technology. Furthermore, the uniform and consistent response of planar and non-planar applications eliminates hardware specialization needs such that modular collision detection systems can be created. The interface electronics and sensor construction is accomplished with commercially producible parts such that retrofitting is easily accomplished. The results support the theoretical relation of compressive stress to measured response in the local frame and the sensor measurements provide a monotonically increasing output as a function of the applied collision force. The novel sensor design in this thesis shows strong promise for a robustly applicable collision detection solution for complex robotic arms and non-standard operating environments.

6.1 Results Summary

The approximate force testing method utilized for characterizing the sensor show the wide dynamic sensing range of the sensor from levels as low 5 N to values as high as 300 N. The strong correlation and consistent results show the sensing to be capable of detecting collision and limiting harm before significant force has occurred to the robotic system or impact object. The force measurement supports and achieved consisten results with the approximate method verifying the measurement. The peak force measurement cover a similar range of 49 N to 419 N. The high level of 419 N clearly demonstrates the sensors collision

detection ability at high levels. The deviation of collision for object impacts which do not squarely impact the sensor–still show a collision detection response.

6.2 Future Work

Further finite element analysis and strain modeling of the system and substrate is necessary to more accurately identify the applicability of the sensor. Specifically, closed cell foam and other elastic substrates experience stress and strain in a nonlinear manner and more complex modeling and force measurement is required to accurately model the system. Additionally, more extensive testing of substrate options to more accurately characterize the effects of material properties on sensor response is needed to increase viability of construction. The testing was primarily carried out using equivalent size elements and objects to maintain continuity of the experimentation. However, additional testing using a variety of not only different sized and shaped elements but also different sized and shaped objects would be beneficial. The collisions utilized for testing were limited to impact collision generated from falling objects. Recall from the previously described hazard origins for mechanical danger, different types of collisions including pinching scenarios, impact and hold scenarios–a collision in which object is already in contact with the sensor and the robotic system actuates towards the object– are necessary to ensure the sensor enables the system to meet current international safety standards including ISO 10218 [22, 23] and IEC 60601-1 [28]. Additional algorithm development for advanced or adaptive collision detection utilizing the sampled signal would also benefit the work. In order to satisfy the previously mentioned standards, routines for online calibration and sensor fault testing are necessary.

Bibliography

[1] A. Mirbagheri, J. Dargahi, F. Aghili, and K. Parsa, "Finite element analysis of a membrane-type piezoelectric tactile sensor with four sensing elements," in *2005 IEEE Sensors*, Nov. 2005, pp. 4 pp.–.

[2] L. Seminara, L. Pinna, M. Valle, L. Basirico, A. Loi, P. Cosseddu, A. Bonfiglio, A. Ascia, M. Biso, A. Ansaldo, D. Ricci, and G. Metta, "Piezoelectric polymer transducer arrays for flexible tactile sensors," in *2012 IEEE Sensors*, Oct. 2012, pp. 1–4.

[3] S. Haddadin, A. Albu-Schaffer, A. De Luca, and G. Hirzinger, "Collision detection and reaction: A contribution to safe physical human-robot interaction," in *IEEE/RSJ International Conference on Intelligent Robots and Systems, IROS 2008*, 2008, pp. 3356–3363.

[4] R. Schulze, T. Gessner, M. Schueller, R. Forke, D. Billep, M. Heinrich, M. Sborikas, and M. Wegener, "Integration of piezoelectric polymer transducers into microsystems for sensing applications," in *Applications of Ferroelectrics held jointly with 2012 European Conference on the Applications of Polar Dielectrics and 2012 International Symp Piezoresponse Force Microscopy and Nanoscale Phenomena in Polar Materials (ISAF/ECAPD/PFM), 2012 Intl Symp*, 2012, pp. 1–4.

[5] A. Yamamoto, S. Nagasawa, H. Yamamoto, and T. Higuchi, "Electrostatic tactile display with thin film slider and its application to tactile telepresentation systems," *IEEE Transactions on Visualization and Computer Graphics*, vol. 12, no. 2, pp. 168–177, 2006.

[6] I. Fujimoto, Y. Yamada, T. Morizono, Y. Umetani, and T. Maeno, "Development of artificial finger skin to detect incipient slip for realization of static friction sensation," in *Proceedings of IEEE International Conference on Multisensor Fusion and Integration for Intelligent Systems, MFI2003.*, Jul. 2003, pp. 15–20.

[7] E. S. Kolesar and C. S. Dyson, "Object imaging with a piezoelectric robotic tactile sensor," *Journal of Microelectromechanical Systems*, vol. 4, no. 2, pp. 87–96, Jun. 1995.

[8] J. M. Wooten, D. M. Bevly, and J. Y. Hung, "Robust large-area piezoelectric polymer based collision detection sensor," in *39th Annual Conference of the IEEE Industrial Electronics Society (IECON-2013), Vienna, Austria,*, Nov. 2013, pp. 1–6.

[9] C. S. Brown, R. C. Kell, R. Taylor, and L. A. Thomas, "Piezoelectric materials, a review of progress," *IRE Transactions on Component Parts*, vol. 9, no. 4, pp. 193–211, 1962.

[10] E. Fukada, "Piezoelectricity of wood," *Journal of the Physical Society of Japan*, vol. 10, no. 2, pp. 149–154, 1955. [Online]. Available: http://jpsj.ipap.jp/link?JPSJ/10/149/

[11] D. Damjanovic, "Ferroelectric, dielectric and piezoelectric properties of ferroelectric thin films and ceramics," *Reports on Progress in Physics*, vol. 61, no. 9, p. 1267, 1998.

[12] E. Fukada, "History and recent progress in piezoelectric polymers," *IEEE Transactions on Ultrasonics, Ferroelectrics and Frequency Control*, vol. 47, no. 6, pp. 1277–1290, Nov. 2000.

[13] H. Kawai, "The piezoelectricity of poly (vinylidene fluoride)," *Japanese Journal of Applied Physics*, vol. 8, no. 7, pp. 975–976, 1969. [Online]. Available: http://jjap.jsap.jp/link?JJAP/8/975/

[14] J. Cai, X. Fu, and H. Liu, "Design of PVdf stress sensor and its application in the stress test of foam plastic," in *2012 International Conference on Measurement, Information and Control (MIC)*, vol. 2, 2012, pp. 821–824.

[15] Y. Shapiro, A. Wolf, and G. Kosa, "Piezoelectric deflection sensor for a bi-bellows actuator," *IEEE/ASME Transactions on Mechatronics*, vol. 18, no. 3, pp. 1226–1230, 2013.

[16] J. Kymissis, C. Kendall, J. Paradiso, and N. Gershenfeld, "Parasitic power harvesting in shoes," in *Second International Symposium on Wearable Computers. Digest of Papers*, 1998, pp. 132–139.

[17] H. Han, Y. Nakagawa, Y. Takai, K. Kikuchi, and S. Tsuchitani, "PVdf film micro fabrication for the robotics skin sensor having flexibility and high sensitivity," in *2011 Fifth International Conference on Sensing Technology (ICST)*, 2011, pp. 603–606.

[18] T. Sekitani, T. Yokota, and T. Someya, "Ultra-flexible, ultra-thin, ultra-sensitive organic pressure sensor system for biomedical applications," in *2012 IEEE Sensors*, 2012, pp. 1–3.

[19] J. Xia, Z. Xie, H. Fang, T. Lan, J. Huang, and H. Liu, "Collision detection of flexible joint manipulator by using joint torque sensors," in *Advanced Intelligent Mechatronics, 2009. AIM 2009. IEEE/ASME International Conference on*, 2009, pp. 1816–1821.

[20] H.-W. Je, J.-Y. Baek, and M.-C. Lee, "A study of the collision detection of robot manipulator without torque sensor," in *ICCAS-SICE, 2009*, 2009, pp. 4468–4471.

[21] L. Seminara, M. Capurro, P. Cirillo, G. Cannata, and M. Valle, "Electromechanical characterization of piezoelectric PVdf polymer films for tactile sensors in robotics applications," *Sensors and Actuators A: Physical*, vol. 169, no. 1, pp. 49–58, 2011.

[22] *Robots and robotic devices - Safety requirements for industrial robots: Part 1: Robots*, International Standard Organization Std. ISO 10 218-1, Rev. E, 2011.

[23] *Robots and robotic devices - Safety requirements for industrial robots: Part 2: Robot systems and integration*, International Standard Organization Std. ISO 10 218-2, Rev. E, 2011.

[24] Y. Roh, V. Varadan, and V. K. Varadan, "Characterization of all the elastic, dielectric, and piezoelectric constants of uniaxially oriented poled PVdf films," *IEEE Transactions on Ultrasonics, Ferroelectrics and Frequency Control*, vol. 49, no. 6, pp. 836–847, 2002.

[25] J. Gere, *Mechanics of Materials*, 5th ed.   Brooks/Cole, 2001.

[26] F. De Lim, L. B. Tan, C. Quan, and T. Y. Tee, "Whole-field board strain and displacement characterization during drop impact using a single camera dic technique," in *2009 11th Electronics Packaging Technology Conference. EPTC '09.*, 2009, pp. 652–655.

[27] J. A. Bryson, "Impact response of polyurethane," Ph.D. dissertation, Washington State University, December 2009.

[28] *Medical electrical equipment - Part 1: General requirements for basic safety and essential performance*, International Electrotechnical Commission Std. IEC 60 601-1, Rev. 3.1, December 2012.

[29] J. Reddy, *An Introduction to Continuum Mechanics.*   Cambridge University Press, 2008.

Appendix A

Material Properties

A.1 Cauchy Stress Tensor

It is important to consider the stress that exists within an object as a *state of stress*. Furthermore, *stress* exists as combination of normal and shear stress components which combine to form a *tensor*. [25]

$$
\underline{\boldsymbol{\sigma}} = \begin{bmatrix} T^{e1} \\ T^{e2} \\ T^{e3} \end{bmatrix} = \begin{bmatrix} \sigma_{11} & \sigma_{12} & \sigma_{13} \\ \sigma_{21} & \sigma_{22} & \sigma_{23} \\ \sigma_{31} & \sigma_{32} & \sigma_{33} \end{bmatrix} = \begin{bmatrix} \sigma_{xx} & \sigma_{xy} & \sigma_{xz} \\ \sigma_{yx} & \sigma_{yy} & \sigma_{yz} \\ \sigma_{zx} & \sigma_{zy} & \sigma_{zz} \end{bmatrix} = \begin{bmatrix} \sigma_x & \tau_{xy} & \tau_{xz} \\ \tau_{yx} & \sigma_y & \tau_{yz} \\ \tau_{xz} & \tau_{yz} & \sigma_z \end{bmatrix} \tag{A.1}
$$

The Cauchy Stress Tensor is one such *state of stress* representation often used in continuum mechanics. In this case, the stress tensor represents the components of stress for an infinitesimally small point in the material and is defined as the *current force* per unit *deformed area*, σ_{ij}. The stress at a point in a three-dimensional continuum can be shown using nine quantities, three per plane, on three mutually perpendicular planes of the point.[29] The stress components for each plane, x,y and z, are combined in Cartesian component form to produce the second-order tensor (A.1).[29] The individual stress vectors, T^{ei}, represent the orthogonal components of stress for each plane. The tensor is utilized to represent complex kinematics and statics in material which exists as a continuous combination of many small infinitesimally small points. The Cauchy Stress tensor is unique because the symmetric properties of the tensor allow for a stress representation of the point using only 6 elements known as a Voigt notation; specifically, σ_x, σ_y, σ_z represent the normal stresses and the shear stresses are represented by σ_{xy}, σ_{xz}, σ_{yz}, or equivalently τ_{xy}, τ_{xz}, or τ_{yz}. The symmetry of

the stress tensor refers to the property: $\sigma_{ij} = \sigma_{ji}$ where i and j represent x, y, or z. This symmetry is particularly useful in the strain modeling to relate experienced stress of the film on the surface of the material to stress components of the continuous material.

A.2 Engineering Strain Tensor

$$\underline{\underline{\epsilon}} = \begin{bmatrix} \epsilon_{11} & \epsilon_{12} & \epsilon_{13} \\ \epsilon_{21} & \epsilon_{22} & \epsilon_{23} \\ \epsilon_{31} & \epsilon_{32} & \epsilon_{33} \end{bmatrix} = \begin{bmatrix} \epsilon_{xx} & \epsilon_{xy} & \epsilon_{xz} \\ \epsilon_{yx} & \epsilon_{yy} & \epsilon_{yz} \\ \epsilon_{zx} & \epsilon_{zy} & \epsilon_{zz} \end{bmatrix} = \begin{bmatrix} \epsilon_x & \frac{\gamma_{xy}}{2} & \frac{\gamma_{xz}}{2} \\ \frac{\gamma_{yx}}{2} & \epsilon_y & \frac{\gamma_{yz}}{2} \\ \frac{\gamma_{xz}}{2} & \frac{\gamma_{zy}}{2} & \epsilon_z \end{bmatrix} \tag{A.2}$$

Strain components of a material use similar notation to stress and results in a *strain tensor*. The *tensor* includes the normal and shear strains. By considering the displacements as small, we can neglect nonlinear terms and the resulting *tensor* known as the *infinitesimal strain tensor* is a symmetric second-order tensor in rectangular Cartesian components. The diagonal components of the tensor ϵ_{11},ϵ_{22}, and ϵ_{23} represent the normal strains and the off diagonal terms ϵ_{12},ϵ_{13}, and ϵ_{23} represent the shear strains. The shear strains are called the *engineering shear strains* and the tensor becomes the *engineering strain tensor* in the final notation [29].

A.3 Geometric Representation of Strain

$$\epsilon_{ij} = \frac{1}{2}(\frac{\delta_i}{j_o} + \frac{\delta_j}{i_o}) \tag{A.3}$$

An important material property for modeling the sensor, the *geometric representation of strain* relates the normal strain to the change of length to the previous length of the material. The combination of change in length in i and j direction represented by δ_i and δ_j respectively divided by the original length j_o and i_o yields the normal strain when divided by 2, ϵ_{ij}.[25] The geometric property is particularly useful when combined with a symmetric strain tensor

because measured surface strains of the film can be transformed to the normal strain of the material.

A.4   Young's Modulus

$$E = \frac{\sigma}{\epsilon} \tag{A.4}$$

The modulus of elasticity introduced by English scientist Thomas Young, Young's Modulus, relates the tension and compression of a material. Specifically, the *Young's Modulus* of a material is the relation of *axial stress* to *axial strain*. The modulus of elasticity is a constant representing the slope of the stress-strain diagram in the linearly elastic region of the graph [25]. The modulus is often used in a form known as *Hooke's law* which more clearly relates the stress of the material due to strain, shown in equation (A.5).

$$\sigma = E\epsilon \tag{A.5}$$

The typical units for E are pascals because strain, ϵ, is a unit less measurement and the SI unit for stress, σ, is pascals or gigapascals.

A.5   Shear Modulus of Elasticity

$$G = \frac{\gamma}{\tau} \tag{A.6}$$

The shear modulus of elasticity is a similar relation to previously discussed *Young's Modulus*. The modulus represents the slope of the linear region of the shear stress-strain curve and is frequently found in the *Hooke's law in shear*, shown in Equation (A.7).

$$\tau = G\gamma \tag{A.7}$$

The shear modulus of elasticity is typically expressed in pascals such that the shear stress, τ, is in the SI unit for stress when the modulus, G, is multiplied times the unit less shear strain, γ [25].